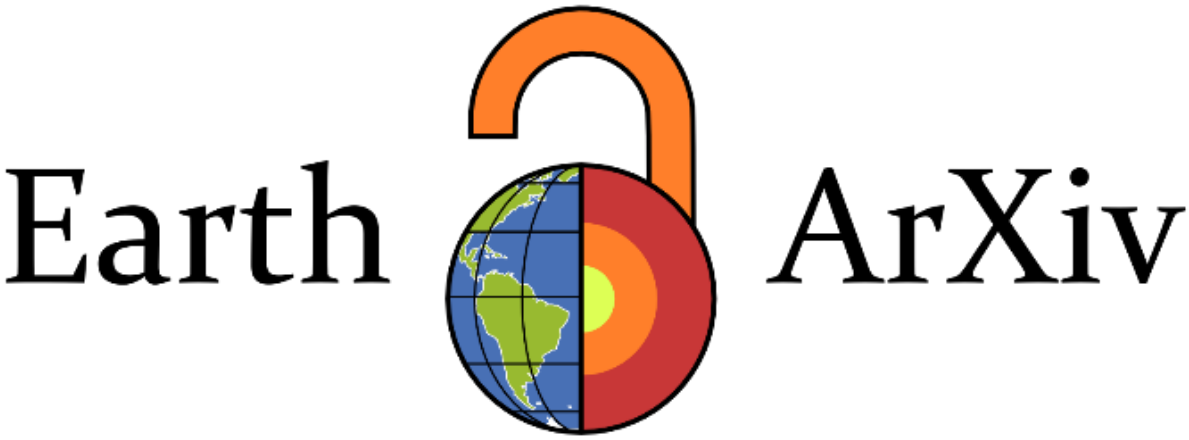

Dust–Cloud Vertical Configurations Influence the Effective Radius of Low-Level Warm Clouds over Marine and Continental Environments

Guoqing Gong[1] and Adeyemi A. Adebiyi[1]

[1] Department of Life and Environmental Sciences, University of California, Merced, USA

Corresponding author: Adeyemi A. Adebiyi (aaadebiyi@ucmerced.edu)

Key Points:

- Dust and cloud vertical configurations modulate dust effects on low-level warm cloud droplet size
- Meteorological variability can obscure a dust-driven tendency toward smaller cloud droplets
- Dust–cloud vertical configuration may reflect distinct microphysical and semi-direct pathways

Abstract

Aerosol–cloud interactions remain a major source of uncertainty in climate forcing estimates, partly because cloud responses depend on the location of aerosols relative to clouds; yet for mineral dust, which accounting for about two-thirds of all aerosol mass, the effects of dust–cloud vertical configuration on cloud droplet effective radius remain unclear. Using multi-year observations from the Atmospheric Radiation Measurement sites at the Eastern North Atlantic (ENA; marine) and Southern Great Plains (SGP; continental), we quantify the sensitivity of low-level warm-cloud effective radius to dust-layer optical depth—the dust aerosol–cloud interaction (dust-ACI) index—for dust located above (Top), within (Middle), and below (Bottom) clouds. These configurations modulate the sign and magnitude of the dust-ACI index. At ENA, the index is strongly positive for the Top configuration (0.130 ± 0.065), weakly positive for the Middle (0.080 ± 0.029), and slightly negative for the Bottom (−0.026 ± 0.021) configuration, whereas the Middle (−0.021 ± 0.057) and Bottom (0.086 ± 0.041) responses reversing signs at SGP. After controlling for meteorological covariability, dust-ACI indices become consistently positive across sites and configurations, revealing that thermodynamic changes associated with vertical configuration can mask an underlying dust microphysical brightening tendency. We propose potential mechanisms whereby dust-induced semi-direct heating dominates in the Top configuration, enhancing stability and suppressing entrainment to yield smaller droplets, whereas the Middle and Bottom configurations reflect competing microphysical and semi-direct pathways whose relative strengths differ between marine and continental regimes. These results show that dust effects on clouds cannot be inferred from dust loading alone, but require accurate representation of dust–cloud vertical configuration and environmental regime.

Plain Language Summary

Dust particles in the atmosphere can modify cloud properties, but their effects depend not only on dust amount, but also on the vertical position of dust relative to clouds. In this study, we use multi-year ground-based observations from a marine site in the Eastern North Atlantic and a continental site in the Southern Great Plains to examine the responses of low-level warm clouds when dust is located above, within, or below the cloud layer. We find that cloud responses vary substantially with dust–cloud vertical configuration. Dust located above clouds, especially over the marine environment, is generally associated with smaller cloud droplets, whereas dust located within or below clouds can produce different responses over marine and continental environments. After accounting for local meteorology, our results suggest that dust generally reduces cloud droplet size, but this effect is masked or even reversed by direct meteorological effects on clouds. This matters because assessments of dust-cloud interactions that consider only the total dust mass may miss the influence of dust-cloud vertical distribution, leading to different estimates of how dust affects cloud droplet size and reflectivity.

1 Introduction

Aerosol–cloud interactions remain one of the largest sources of uncertainty in estimates of climate sensitivity and radiative forcing, exceeding even those associated with greenhouse gas forcing (Bender, 2020; Im et al., 2026; Watson-Parris & Smith, 2022). This is because aerosols influence the Earth's radiation budget through multiple interacting pathways that depend strongly on environmental conditions (Yu et al., 2024). Aerosols exert direct radiative effects by scattering and absorbing solar and terrestrial radiation, thereby modifying the atmospheric energy budget independently of clouds (Li et al., 2022). They also induce semi-direct effects (SDE), in which heating by absorbing aerosols perturbs atmospheric stability, cloud fraction, and cloud vertical structure (Adebiyi et al., 2015; Koch & Del Genio, 2010; Pandey & Adebiyi, 2026b). In addition, aerosols can modify cloud microphysics through indirect effects (IDE), altering cloud droplet number concentration, cloud droplet effective radius (R_e), and cloud lifetime (Patnaude & Diao, 2020; Qiu et al., 2024; Twomey, 1977). These processes are particularly consequential for low-level warm clouds, which exert a strong cooling influence on the climate system due to their high albedo and widespread coverage (Voigt et al., 2021). Because these clouds are tightly coupled to boundary-layer thermodynamics and aerosol conditions, even modest aerosol perturbations can produce substantial radiative impacts (Bellouin et al., 2020). As a result, constraining aerosol–cloud interactions in low-level warm clouds is essential for narrowing uncertainties in climate sensitivity and radiative forcing (Bellouin et al., 2020).

The magnitude and sign of aerosol effects on clouds depend strongly on the vertical distribution of aerosols relative to cloud layers, as well as on the environmental setting in which the interaction occurs (Adebiyi et al., 2015; Lin et al., 2023). For absorbing aerosols, the semi-direct effect is especially sensitive to aerosol–cloud geometry because the location of radiative heating determines the thermodynamic response of the surrounding atmosphere (Pandey & Adebiyi, 2026a, 2026b). Specifically, when an absorbing aerosol layer is located above clouds, solar absorption within the elevated layer warms the free troposphere and increases lower-tropospheric stability, which can suppress cloud-top entrainment and enhance cloud persistence or cloud fraction (Pandey & Adebiyi, 2026a; Wilcox, 2010). In contrast, when absorbing aerosols are embedded within the cloud layer, localized radiative heating can promote evaporation of cloud droplets and destabilize the cloud structure, potentially leading to partial cloud dissipation (Koch & Del Genio, 2010; Kok et al., 2023). When aerosols are located below the cloud, radiative heating in the sub-cloud layer may enhance turbulence and vertical moisture transport, thereby indirectly influencing cloud development by modifying boundary-layer thermodynamics (McFarquhar & Wang, 2006). In addition to these semi-direct pathways, indirect effects can occur when aerosols are present within or below low-level clouds, where they act as cloud condensation

nuclei and influence cloud droplet sizes. The relative importance of these mechanisms differs between marine and continental environments. For example, indirect effects tend to be stronger over land, where background CCN concentrations are higher, and cloud microphysics are more responsive to aerosol perturbations than over the ocean (Lohmann & Lesins, 2003; Yang et al., 2022). These contrasts suggest that identical aerosol–cloud vertical configurations may produce different cloud responses over ocean and land.

Mineral dust, a major contributor to global aerosol mass (Kim et al., 2014), accounts for approximately one-third of global aerosol shortwave absorption (Sand et al., 2021). Unlike other absorbing aerosols, dust particles span more than three orders of magnitude in size, from submicron to coarse, a range that enables dust to interact with both shortwave and longwave radiation (Adebiyi & Kok, 2020; Adebiyi et al., 2023; Kok et al., 2023). In addition, large quantities of dust are transported westward from the North African deserts across the North Atlantic Ocean and onward toward the Caribbean and North America (Fig. 1a). Additional dust sources over the North American continent contribute to the local aerosol burden over the continent's interior (Kok et al., 2021). Over specific regions of the North Atlantic Ocean and North America, previous studies have examined dust impacts on cloud microphysics or radiative effects (Amiri-Farahani et al., 2017; Huang et al., 2019; Song et al., 2018; Zheng et al., 2020), but few have systematically compared cloud responses across distinct vertical arrangements such as dust above, within, or below clouds (Lin et al., 2023; Pandey & Adebiyi, 2026a). Moreover, most of these studies rely on satellite observations, which provide broad spatial coverage but limited temporal continuity and often insufficient vertical resolution to fully resolve dust–cloud overlap (Jia et al., 2021; Painemal et al., 2020). Even fewer studies have contrasted cloud response between marine and continental environments, where differences in thermodynamic state, background aerosol composition, and boundary-layer dynamics may cause identical dust–cloud vertical geometries to produce qualitatively different cloud responses (Jia et al., 2019; X. Ma et al., 2018; Su et al., 2024).

To address these gaps, we use the multi-year, continuous, ground-based observations from the U.S. Department of Energy's Atmospheric Radiation Measurement (ARM) program at two contrasting sites: the Eastern North Atlantic (ENA, marine) and the Southern Great Plains (SGP, continental). These two sites represent typical marine and continental settings, and the large-scale aerosol and cloud environments over the two regions are shown in Fig. 1a. The transport pathways to these two locations differ substantially. Dust reaching the ENA typically undergoes long-distance transport across the Atlantic Ocean or directly from northern Sahara dust sources, with a substantial fraction arriving at elevated layers (Wang et al., 2020). By contrast, dust reaching the SGP is more commonly associated with regional emission events and is frequently confined to the lower

troposphere (Evans, 2025; Lambert et al., 2020). Because these two locations are not directly along the major dust transport pathways, overall dust concentrations and frequency of occurrence are generally low, partially limiting analysis of dust–cloud interactions. Despite the limited occurrence and abundance, the two sites together provide an opportunity to examine how dust–cloud vertical configuration modulates cloud microphysical responses across contrasting environments. Leveraging these multi-year ARM datasets, we show that dust aerosol–cloud interactions and the associated response of cloud droplet effective radius to dust vary depending on whether dust resides above, within, or below the cloud layers, and that these responses diverge substantially between marine and continental regimes.

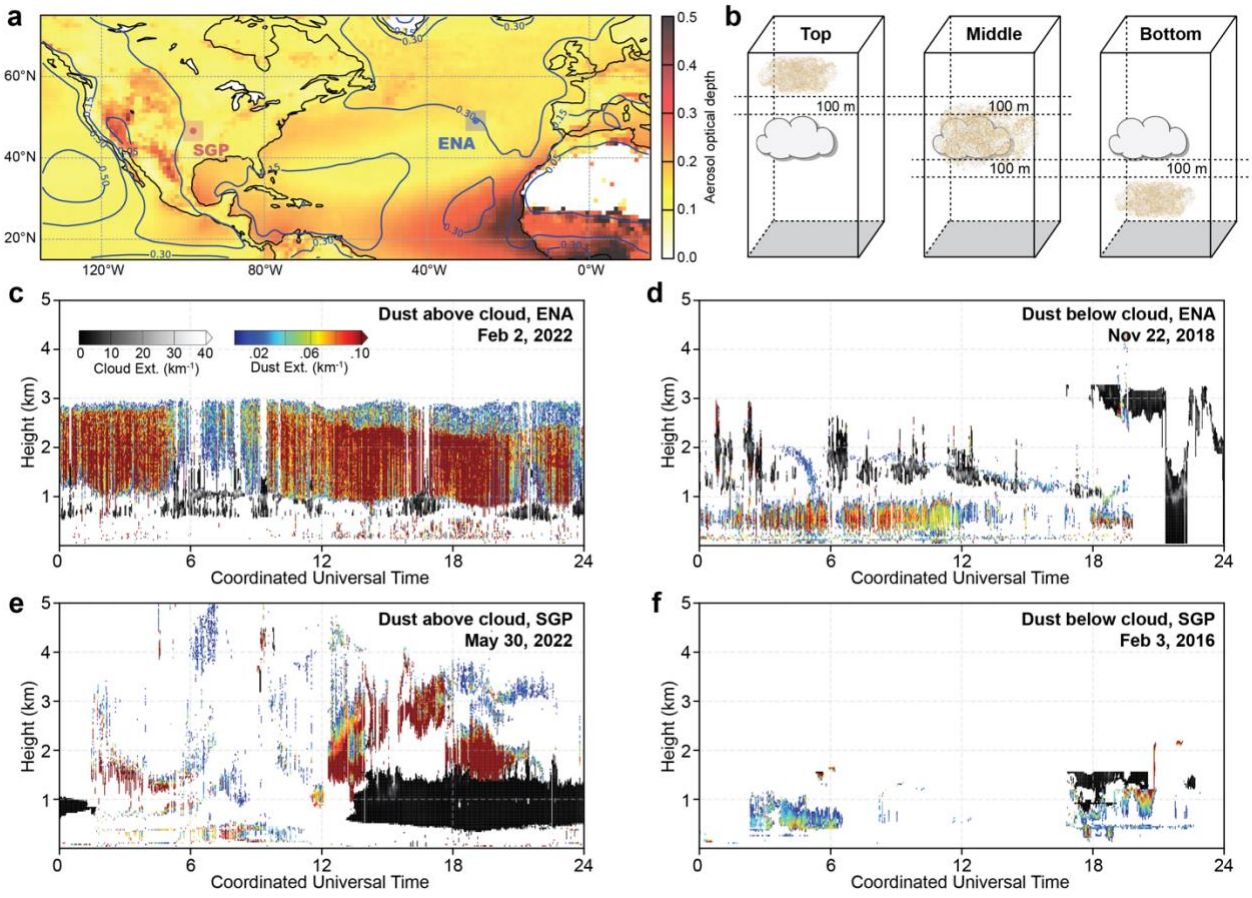

Figure 1. Overview of the observational context, dust–cloud configuration framework, and representative cases used in this study. (a) Climatological aerosol optical depth and single-layer low-level warm cloud fraction (contours) derived from MODIS for 2000–2012. The locations of the ARM ENA (blue) and SGP (red) sites are marked, and the shaded boxes denote the 5° × 5° regions centered on each site used for satellite data collocation (see Text S1 and Fig. S1). (b) Concept illustration of the three dust-cloud configurations (Top, Middle, and Bottom) used in this study, defined based on the relative vertical positions of dust layers

and cloud layers. Dashed lines indicate the vertical separation thresholds (±100 m) used to classify the configurations. Example cases of (c) the Top configuration (February 2, 2022) and (d) the Bottom configuration (November 22, 2018) at ENA. Example cases of (e) the Top configuration (May 30, 2022) and (f) the Bottom configuration (February 3, 2016) at SGP.

2 Data and Methods

2.1 Identifying dust and cloud layers

Aerosol information was obtained from the Raman Lidar Profiles-Feature detection and Extinction (RLPROF-FEX) Value-Added Product at ENA and SGP sites between January 1, 2016, and December 31, 2025, corresponding to the maximum continuous overlapping period for both sites. RLPROF-FEX provides aerosol optical properties, including aerosol extinction, depolarization ratio, scattering ratio, and a feature mask for identifying aerosol layers. The product has a temporal resolution of 2-min and a vertical resolution of 30-m, with 667 vertical levels, making it suitable for characterizing the vertical structure of dust aerosols (Chand et al., 2023). To obtain reliable dust aerosol information, we followed the product documentation and applied several quality-control criteria (Chand et al., 2023). Specifically, we retained only profiles identified as aerosol by the feature mask, used observations with total detection confidence greater than 0.3, and excluded retrievals with poor quality ($quality\ flag \neq 0$). To avoid potential contamination of dust retrievals by precipitation, profiles were removed if any height level within a given profile was flagged as rain by the feature mask. Because incomplete near-surface lidar overlap can degrade Raman lidar signal quality and lead to unstable retrievals, particularly within the lowest 0–0.03 km, data below 0.03 km were excluded (Thorsen et al., 2015). The upper altitude limit was set to 8 km to reduce the influence of low signal-to-noise ratios at higher altitudes on aerosol extinction and depolarization retrievals (Newsom et al., 2022). The 0.03–8 km range captures most tropospheric dust layers relevant to interactions with low-level warm clouds and is consistent with commonly used altitude ranges in Raman lidar aerosol studies (Chand et al., 2023). After applying these filters, 1,032,345 and 1,920,230 valid aerosol profiles were retained at ENA and SGP, respectively.

To isolate the dust component from total aerosol extinction, we first calculated the particle depolarization ratio (PDR) using the scattering ratio and observed depolarization ratio provided by RLPROF-FEX. Dust particles are typically highly nonspherical and therefore exhibit higher depolarization ratios than most non-dust aerosols, making depolarization information an effective indicator for dust identification (Noh et al., 2017). However, the observed depolarization ratio includes contributions from both particle and molecular scattering, particularly under conditions of low aerosol loading or at higher altitudes. Direct use of the observed depolarization ratio may therefore underestimate the contribution of

nonspherical dust particles. To reduce this effect, the observed depolarization ratio was corrected using the scattering ratio to derive PDR (Burton et al., 2015):

$$t = S + S\delta_m - \delta_m$$

$$x_{num} = t\delta_{aerosol} - \delta_m$$

$$x_{den} = S - 1 + S\delta_m - \delta_{aerosol}$$

$$PDR = \frac{x_{num}}{x_{den}}$$

where S is the scattering ratio, $\delta_{aerosol}$ is the observed depolarization ratio, and $\delta_m = 0.0049$ is the molecular depolarization (Behrendt & Nakamura, 2002). The corrected PDR more directly reflects particle shape characteristics and is therefore more suitable for distinguishing dust from non-dust aerosols.

Under the external mixing assumption (Mamouri & Ansmann, 2014), aerosols were treated as a mixture of dust and non-dust components. The dust fraction, f_{dust}, was then estimated using a depolarization mixing relationship based on reference depolarization values for non-dust and pure dust particles (Freudenthaler et al., 2009; Noh et al., 2017).

$$f_{dust} = \begin{cases} 1, & PDR \geq \delta_d \\ 0, & PDR \leq \delta_{nd} \\ \dfrac{(PDR - \delta_{nd})(1 + \delta_d)}{(\delta_d - \delta_{nd})(1 + PDR)}, & \delta_{nd} < PDR < \delta_d \end{cases}$$

where $\delta_{nd} = 0.15$ and $\delta_d = 0.31$ represent the reference values for non-dust and pure dust, respectively (Proestakis et al., 2024; Soupiona et al., 2020). This approach allows a continuous representation of mixed dust and non-dust conditions, thereby avoiding the potential bias introduced by simple threshold-based classification under aerosol mixing states. Dust extinction was then calculated as:

$$ext_{dust}(z) = f_{dust}(z) \times ext_{aerosol}(z)$$

where $ext_{aerosol}(z)$ is the total aerosol extinction from RLPROF-FEX. To reduce the influence of cloud contamination and nonphysical retrievals, only extinction values less than 1.25 km^{-1} were retained (Kacenelenbogen et al., 2014), a threshold commonly used to distinguish aerosol from cloud signals. After the PDR-based dust-fraction retrieval and extinction filtering, 279,784 and 532,920 valid dust-aerosol profiles were retained at ENA and SGP, respectively. For each valid dust-aerosol profile, the dust layer was identified as the vertically continuous range with valid dust extinction. Dust-layer optical depth was calculated by vertically integrating dust extinction within the identified dust layer:

$$DLOD = \int_{z_{DBH}}^{z_{DTH}} ext_{dust}(z)dz$$

where z_{DBH} and z_{DTH} denote the dust-layer base height (DBH) and dust-layer top height (DTH), respectively. If multiple dust layers were present within a single profile, the layer with the largest DLOD was selected as the dominant dust layer for subsequent analysis (Haarig et al., 2022). Dust-layer thickness was defined as $z_{DTH} - z_{DBH}$, and dust-layer mean height was defined as $(z_{DTH} + z_{DBH})/2$.

Cloud macrophysical properties, including cloud base height (CBH), cloud top height (CTH), and number of cloud layers, were obtained from the Active Remote Sensing of Clouds (ARSCL) Value-Added Product. ARSCL integrates active remote sensing measurements from millimeter-wavelength cloud radar, lidar, and ceilometer observations to objectively characterize the vertical distribution of hydrometeors, making it suitable for identifying cloud boundaries (Clothiaux et al., 2001). The product has a temporal resolution of 4-s and 10 cloud layers, including the CBH and CTH of each layer. To match the temporal resolution of RLPROF-FEX, ARSCL was resampled to a 2-min resolution. To avoid ambiguity in matching cloud layers with dust layers under multilayer cloud conditions, this study retained only single-layer cloud cases. The CBH and CTH were used to define the vertical extent of the single cloud layer, and the cloud-layer mean height was defined as the midpoint between CBH and CTH. Single-layer warm clouds were identified by matching the CTH of each cloud layer to the corresponding RLPROF-FEX temperature profile and retaining only cases where the cloud-top temperature was above 0 °C.

Cloud optical and microphysical properties, including cloud droplet effective radius (R_e), cloud fraction, and liquid water path (LWP), were obtained from the Multifilter Rotating Shadowband Radiometer Cloud Optical Depth (MFRSRCLDOD) Value-Added Product. This product retrieves cloud optical depth from MFRSR shortwave radiation measurements and estimates LWP and R_e using radiative transfer calculations (Turner et al., 2014). It is primarily applicable to single-layer, horizontally homogeneous warm-cloud conditions (Turner et al., 2014). This product has a temporal resolution of 20-s and was averaged to 2-min intervals to match RLPROF-FEX and ARSCL. Following the product documentation, samples with LWP < 20 g m^{-2} were excluded because of large retrieval uncertainty (Zheng et al., 2020), whereas samples with LWP > 300 g m^{-2} were removed to reduce potential precipitation influence (Zheng et al., 2020). Only cases with cloud fraction > 0.9 were retained to ensure horizontally homogeneous cloud conditions (Turner et al., 2014). After applying these filters, 49,719 and 19,631 valid single-layer warm-cloud samples were retained at ENA and SGP, respectively.

The single-layer warm-cloud samples were then temporally matched with valid dust profiles to construct the dust–cloud collocation dataset. A collocated period was defined as a continuous sequence of 2-min timestamps during which both valid dust profiles and

valid single-layer warm-cloud observations were available. A sample was retained only when valid dust and cloud information were present at the same 2-min timestamp. To focus on low-level warm clouds, collocated samples were further retained only when CTH was below 3 km (McHardy et al., 2018; Xi et al., 2022). After applying these collocations and low-cloud filters, the final dust–cloud collocation dataset included 3,994 samples at ENA and 934 samples at SGP.

To provide an independent comparison with the ground-based ARM observations, we also constructed a satellite-based dust–cloud collocation dataset. The detailed procedure for identifying dust and cloud layers from satellite observations, including the satellite–site sampling domain, satellite collocation procedure, and low-level warm-cloud screening, is described in Text S1. This procedure yielded 720 and 316 satellite-based dust–cloud collocation samples at ENA and SGP, respectively. Because the satellite and ARM observations view the dust–cloud system from opposite directions, they provide complementary constraints but are also subject to different attenuation-related uncertainties. For ground-based lidar, uncertainties are generally larger when retrieving dust layers above clouds because the lidar signal must pass through the cloud before reaching the overlying aerosol layer. In contrast, for satellite-based lidar, uncertainties are generally larger when retrieving dust layers below clouds because the lidar signal is attenuated by the cloud before reaching the underlying aerosol layer (Kim et al., 2008). Despite these platform-dependent limitations, the satellite observations provide an independent dataset for evaluating whether the cloud responses inferred from the ground-based ARM observations are consistent across observing systems.

2.2 Obtaining dust–cloud configuration

A unified framework was used to classify the relative vertical position of dust and cloud based on dust- and cloud-layer heights (Fig. 1b). For each collocated sample, the corresponding CBH, CTH, DBH, and DTH were used to determine the dust–cloud vertical configuration. Thus, each 2-min sample was classified into the Top, Middle, or Bottom configuration according to the relative positions of the dust and cloud layer boundaries. This sample-level classification preserves the observed dust–cloud geometry at each timestamp and avoids imposing a single representative category on samples that may experience short-term changes in cloud or dust-layer height. Such an approach is consistent with previous profile-based aerosol–cloud studies (Hong & Di Girolamo, 2022; Mann et al., 2014). When the dust base is at least 100 m above the cloud top, the case is classified as “Top”, indicating dust above the cloud. When the dust layer overlaps the cloud layer, allowing the dust-layer top to extend up to 100 m above the cloud top and the dust-layer base to extend up to 100 m below the cloud base, it is classified as “Middle”. When the dust layer is entirely

below the cloud, with its top at least 100 m below the cloud base, it is classified as "Bottom". This classification captures three typical dust–cloud configurations. A ±100 m threshold is used to reduce the impact of retrieval uncertainty and avoid misclassification due to small height variations. The same criteria are applied to both ARM and satellite data to ensure consistency and comparability across platforms. Representative ARM cases are shown in Figure 1c–f to illustrate how different dust–cloud vertical configurations appear in observations. Figure 1c and 1d show Top and Bottom cases at ENA, respectively, whereas Figure 1e and f show Top and Bottom cases at SGP, respectively. The red boxes indicate the height and time ranges of the dominant dust layer.

This classification framework was then applied to the dust–cloud collocation samples. For the ground-based ARM observations, 236, 1,216, and 2,206 of the 3,994 ENA collocated samples were classified as Top, Middle, and Bottom, respectively. At SGP, 8, 305, and 607 of the 934 collocated samples were classified as Top, Middle, and Bottom, respectively. For the satellite observations, 339, 41, and 112 of the 720 ENA collocated samples were classified as Top, Middle, and Bottom, respectively, whereas 85, 24, and 57 of the 316 SGP collocated samples were classified into the same three categories. Samples that represented transitional geometries or did not satisfy the geometric criteria for the three typical configurations were excluded from subsequent analyses.

2.3 Estimating cloud response to dust

To quantify the impact of dust on cloud responses, we estimate the dust aerosol–cloud interaction (dust-ACI) index as the sensitivity of cloud droplet effective radius (R_e) to dust-layer optical depth (DLOD), evaluated using a log–log regression applied separately to each dust–cloud configuration, defined as:

$$\beta_{R_e-DLOD} = -\frac{\partial ln(R_e)}{\partial ln(DLOD)}$$

where $ln(R_e)$ and $ln(DLOD)$ denote the natural-log-transformed cloud droplet effective radius and dust-layer optical depth, respectively. Both variables were standardized before regression to allow direct comparison of regression coefficients. β_{R_e-DLOD} is the dust-ACI index. The negative sign ensures that a decrease in R_e with increasing DLOD yields a positive value, consistent with the Twomey effect. To isolate microphysical responses under comparable cloud water conditions, the analysis was repeated within three LWP ranges (20–60, 60–100, and >100 g m^{-2}). The regression was performed separately within each LWP bin. These LWP ranges were selected to control for the direct influence of LWP on R_e and to distinguish dust-ACI sensitivities under thin, moderately thick, and thicker liquid-cloud conditions. The first two bins are consistent with LWP ranges commonly used in

aerosol–cloud interaction studies (Jia et al., 2019; X. Ma et al., 2018), whereas higher-LWP conditions were combined into a single bin of >100 g m^{-2} to retain sufficient samples after further stratification by dust–cloud vertical configuration. For all regressions, 95% confidence intervals derived from the standard errors were used to quantify statistical uncertainty.

2.4 Effects of meteorology on cloud response to DLOD

To separate the effects of dust and meteorology on cloud microphysics, we incorporated meteorological variables from ARM radiosonde and Doppler lidar products. Thermodynamic and horizontal-wind variables were obtained from the Gridded Sonde (SONDEGRID) Value-Added Product, which is based on standard ARM radiosonde observations and provides time–height fields at 1-min temporal resolution and 20-m vertical resolution (Fairless et al., 2021). This structure makes SONDEGRID suitable for collocation with other ARM products. Specifically, we extracted relative humidity (RH), temperature (T), potential temperature, and wind speed from SONDEGRID. Vertical-motion information was obtained from the Doppler Lidar Vertical Velocity Statistics Value-Added Product, which provides Doppler-lidar-retrieved vertical velocity at 10-min temporal resolution and 30-m vertical resolution. These variables were used to characterize the thermodynamic and dynamic background near low-level warm clouds. All meteorological variables were linearly interpolated to 2-min intervals to match the RLPROF-FEX observations.

Candidate meteorological variables were selected based on both physical relevance and statistical redundancy. RH, T, vertical wind shear (VWS), vertical velocity (VV), and lower-tropospheric stability (LTS) represent moisture conditions, thermal state, dynamical shear, vertical motion, and lower-tropospheric stability, respectively, thereby covering the main meteorological pathways that can modulate cloud droplet effective radius (Su et al., 2024; Wall et al., 2022). Because variables at different levels may contain redundant information, we examined collinearity among candidate variables using correlation matrices and retained representative variables that were most consistent with the height range of low-level warm clouds and had the most direct physical interpretation (see Text S2 and Fig. S2 for details). Specifically, RH and T were averaged over 750–850 hPa ($RH_{750–850}$ and $T_{750–850}$) to represent humidity and temperature near the cloud layer. Higher RH can help maintain liquid cloud water, whereas temperature variations can influence condensation, evaporation, and both the retrieval and physical variability of R_e (Chen et al., 2008; Martins et al., 2011). VWS was defined as the zonal wind-speed difference between 725 and 925 hPa ($VWS_{725–925}$) to characterize dynamical mixing across the cloud layer; stronger wind shear may modify cloud-top entrainment and aerosol–cloud contact efficiency (Fan et al., 2009; Yamaguchi et al., 2019). VV was averaged over 750–850 hPa ($VV_{750–850}$) to represent upward

or downward motion near the cloud layer. Upward motion generally favors water vapor condensation and droplet growth, whereas subsidence can enhance evaporation or suppress cloud development (Peng et al., 2005). LTS_{700} was defined as the difference between the potential temperature at 700 hPa and the near-surface potential temperature and was used to describe lower-tropospheric stability. Stronger stability generally limits vertical mixing and may alter cloud-top entrainment and boundary-layer moisture structure (Wang et al., 2023; Wood & Bretherton, 2006). This variable selection is also consistent with previous aerosol–cloud interaction studies that controlled for near-cloud humidity, stability, wind shear, and vertical motion (Su et al., 2024; Wall et al., 2022).

For each dust–cloud vertical configuration, a multiple linear regression model was applied to quantify the joint effects of dust and meteorological conditions on R_e:

$$ln(R_e) = \alpha_0 + b^*_{R_e-DLOD} ln(DLOD) + \sum_i \alpha_{R_e-x_i} X_i + \epsilon$$

where α_0 is the intercept, ϵ is the residual term, and X_i represents the meteorological variables (i.e., $RH_{750–850}$, $T_{750–850}$, LTS_{700}, $VWS_{725–925}$, $VV_{750–850}$). To facilitate comparison of the relative effects of different predictors, $ln(R_e)$, $ln(DLOD)$, and all meteorological variables were standardized prior to regression. The resulting coefficients, therefore, represent standardized regression coefficients. Specifically, $b^*_{R_e-DLOD}$ denotes the standardized regression coefficient of $ln(DLOD)$ on $ln(R_e)$ after controlling for meteorological factors, whereas $\alpha_{R_e-x_i}$ represents the standardized regression coefficient of each meteorological variable (X_i) on $ln(R_e)$. To remain consistent with the dust-ACI definition introduced above, the dust-ACI index with minimized meteorological modulation was defined as:

$$\beta^*_{R_e-DLOD} = -b^*_{R_e-DLOD}$$

Thus, the original β_{R_e-DLOD} represents the dust-ACI index derived from the bivariate regression (see Section 2.3). Because this regression does not explicitly account for meteorological covariability, β_{R_e-DLOD} likely reflects both dust-related effects and variations in the meteorological background. In contrast, $\beta^*_{Re-DLOD}$ represents the independent contribution of DLOD to R_e after controlling for meteorological variables and is used to characterize the dust-ACI index after minimizing the influence of meteorology. Therefore, comparing their difference ($\beta_{R_e-DLOD} - \beta^*_{R_e-DLOD}$) allows us to estimate the extent to which meteorological conditions modulate, enhance, or suppress the apparent dust–cloud interaction inferred from the bivariate regression. Similarly, to show the sensitivity of R_e to meteorological conditions compared to the dust-ACI index, we present the result as negative $\alpha_{R_e-x_i}$.

3 Results

3.1 Characteristics of dust–cloud configurations

Over the ENA and SGP, we find that dust aerosols are more likely to occur below (Bottom) and within (Middle) low-level clouds than above them (Top). Specifically, at ENA, 3,994 valid dust–cloud matched samples were identified, of which 3,658 were assigned to one of the three configurations. The remaining matched samples were valid collocations but did not meet the criteria for the three configuration categories (see Section 2.2). Among the classified samples, 60.3% are Bottom configuration, 33.2% are Middle configuration, and 6.5% are Top configuration (Fig. 2a). Because of the stringent criteria required for the dust–cloud configurations (see Sections 2.1 and 2.2 above), the number of Top configuration cases is limited (see Fig. S3a). Similarly, at SGP, 934 valid dust–cloud matched samples were identified, of which 920 met the classification criteria (see Section 2.2) and were assigned to one of the three configurations: 66.0%, 33.2%, and 0.9% were Bottom, Middle, and Top configurations, respectively (Fig. 2a). Because the Top configuration has a small percentage (only eight samples) at SGP, we exclude this category from subsequent analysis. Between the Bottom and Middle configurations that dominate the overall dust–cloud vertical distributions, winter is the only season in which the Middle configuration occurs more frequently than the Bottom configuration (Fig. S3a). Overall, the median DLOD for the Top configuration is higher than those of the Middle and Bottom configurations by factors of 2 and 3, respectively, despite its limited occurrence at the ENA site (Fig. 2b). Similarly, the median DLOD over SGP for the Middle configuration is a factor 1.7 higher than the Bottom configuration (Fig. 2f).

Relative to the ground-based lidar observations at ENA and SGP, the infrequent overpass of satellite-based lidar observations has a higher frequency of occurrence for the Top configurations over ENA (68.9%) and SGP (51.2%) than Middle and Bottom (Fig. S4a). This is expected given the satellite sensor's scanning direction, which often results in higher uncertainties where signal attenuation is greater – that is, dust below and within the cloud for CALIPSO (Liu et al., 2009). The dominant configurations, Top and Bottom, show opposite seasonal patterns between ENA and SGP: Top is more frequent at ENA in spring and summer, whereas Bottom is more frequent at ENA in fall and winter (Fig. S3b). In contrast to ENA, the occurrence frequency at SGP is higher for the Bottom configuration in spring and summer and for the Top configuration in fall and winter (Fig. S3b). This satellite-based frequency of occurrence for Bottom configuration is consistent with ground-based lidar observation at SGP (Fig. S3a and 3b). Furthermore, DLOD magnitude also varies by dust–cloud vertical configuration. Although Top configurations occur most frequently, higher DLOD values are generally found when dust is within or below clouds (Fig. S4b). This pattern

may partly reflect lidar detection selectivity. For CALIPSO, which observes from above, cloud attenuation can make dust below or within clouds more difficult to detect unless the dust layer is optically thick. Conversely, for ground-based ARM lidar, dust above clouds can be more difficult to detect consistently because cloud layers may attenuate the upward-looking lidar signal. Thus, the configurations that are less favorable for each lidar viewing geometry tend to show higher DLOD, suggesting that configuration-dependent DLOD differences reflect both physical dust loading and retrieval sensitivity.

The site-to-site differences in dust–cloud configuration frequencies are consistent with distinct background vertical structures of dust and clouds at ENA and SGP. At ENA, dust-layer height shows two distinct peaks, with a stronger peak near 800 m (Fig. 2c), whereas at SGP, dust is primarily concentrated near the surface, at approximately 200 m (Fig. 2g). Clouds at ENA are mainly confined to a narrower height range, while those at SGP span a broader vertical range (Fig. 2c and 2g). These contrasting dust and cloud height distributions help explain why Bottom and Middle configurations dominate at both sites, while Top cases are relatively rare, especially at SGP. Because these configurations represent distinct dust–cloud vertical contexts, we next examine whether cloud properties vary systematically among them. We find that these dust–cloud configurations exhibit distinct cloud properties, including R_e and LWP. Specifically, the probability distributions indicate that the median LWP for the Middle configurations (95.8 and 113.3 g m^{-2}) is higher over both ENA and SGP than those for the Top (48.4 g m^{-2} for ENA) and Bottom (61.3 and 88.4 g m^{-2}) configurations (Fig. 2d and 2h). As a function of season, both the Middle and Bottom show relatively higher LWP values in spring and fall than in summer and winter at the ENA and SGP sites (blue lines in Fig. 2j). There are also distinct changes in R_e across the different dust-cloud configurations at both ENA and SGP. Specifically, the median values of R_e for the Top configuration (14.9 μm for ENA) are higher than the Middle (13.1 and 10.1 μm), which are higher than the Bottom configurations (11.9 and 8.2 μm), across both sites (Fig. 2e and 2i). In addition, seasonal variations in R_e show contrasting patterns between the two sites: for both the Middle and Bottom configurations, R_e is highest in winter and lowest in summer at ENA, whereas it is generally higher in summer–autumn than in winter–spring at SGP (black lines in Fig. 2j).

Our result also shows differences in the mean height and geometric thickness of the cloud layer over both ENA and SGP, with seasonal variability differing from that of LWP and R_e (see Fig. 2j). Specifically, we find that the Middle configurations generally have low-level clouds that are geometrically thicker (0.93 and 1.13 km) than Bottom (0.60 and 0.59 km) and Top (0.46 km for ENA) configurations over both ENA and SGP. These differences in geometric cloud thickness are consistent with differences in LWP and R_e, particularly between the Middle and Bottom configurations. Specifically, thicker clouds with higher LWP and R_e

occur in the Middle configuration than in the Bottom configuration across seasons (Fig. 2j). In addition, the mean cloud heights (defined as the mean of cloud base and top heights) are higher for Bottom configurations than for Top and Middle configurations (Fig. 2j). This is because of the higher cloud-base height, leading to a larger difference in cloud-base heights among the configurations than in cloud-top heights, which is likely associated with radiative warming by shortwave-absorbing dust aerosols in the boundary layer or stronger vertical wind shear resulting in stronger boundary-layer turbulence (Bottom higher than Middle). Overall, the different dust-cloud configurations exhibit distinct mean cloud properties, with differences between land and ocean, suggesting differences in cloud responses to dust.

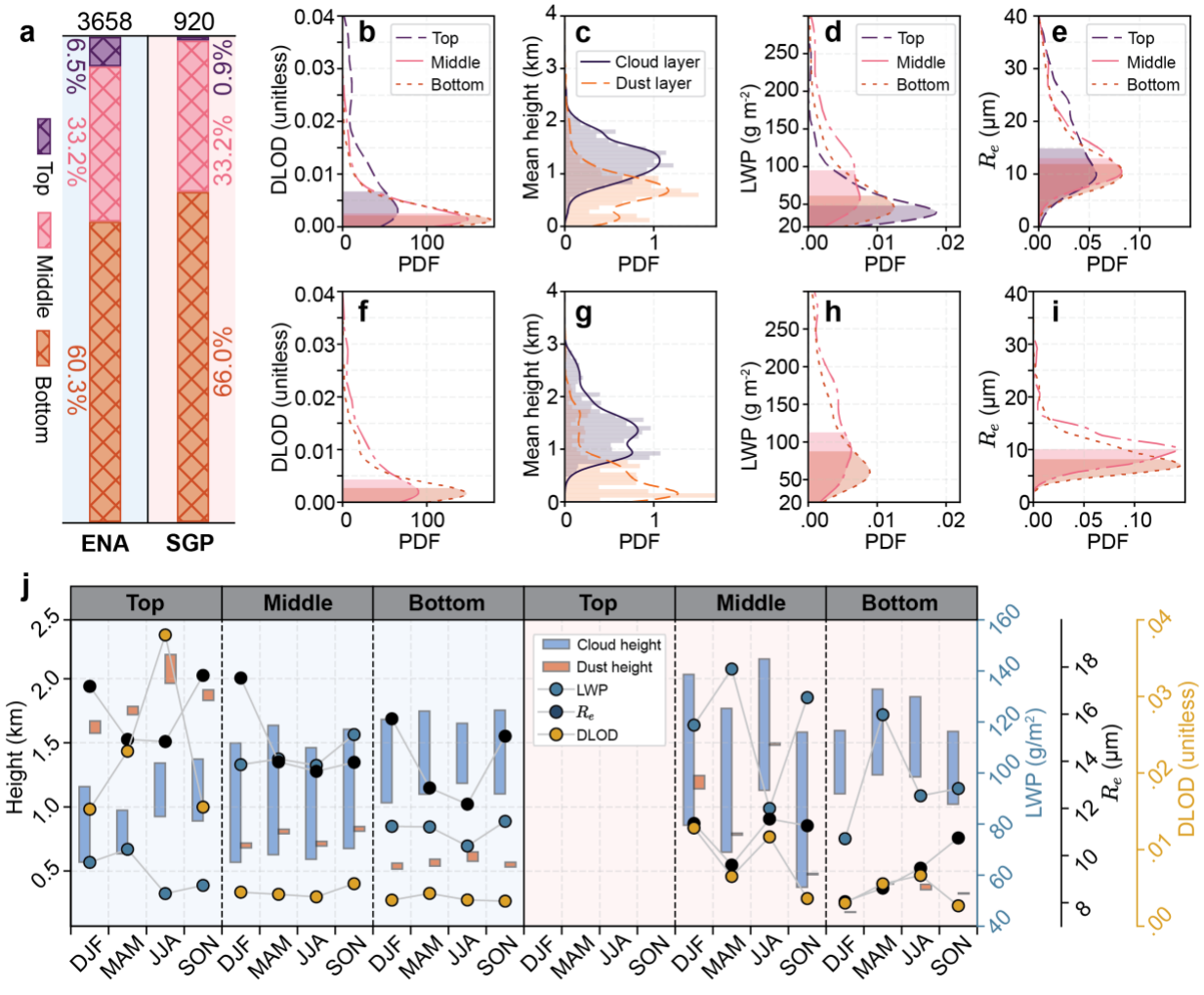

Figure 2. Dust–cloud vertical configurations and associated properties at ENA and SGP. (a) Fractional and total occurrence of Top, Middle, and Bottom configurations at ENA and SGP. (b) Probability density functions (PDF) of dust-layer optical depth (DLOD) at ENA. (c) PDF of cloud- and dust-layer heights during dust–cloud colocation at ENA. (d, e) PDF of liquid water path (LWP) and cloud droplet effective radius (R_e) at ENA. (f–i) Same as (b–e), but for SGP. Shaded areas indicate the lower 50% of each distribution. (j) Seasonal variations in cloud

height, dust height, LWP, R_e, and DLOD for each vertical configuration at ENA (blue background) and SGP (red background), shaded bars denote cloud and dust vertical ranges, and markers indicate seasonal mean cloud and dust properties.

3.2 Cloud Response to Dust-Cloud Configurations

To better understand the cloud response to dust, we estimate dust aerosol–cloud interaction (dust-ACI) index as the sensitivity of cloud droplet effective radius to dust-layer optical depth (β_{R_e-DLOD}; see Section 2.3 above), and find a marked difference in cloud response across different dust–cloud vertical configurations and across marine and continental environments (Fig. 3). At ENA (marine environment; Fig. 3a), our results show a strong positive dust-ACI index for the Top configuration (0.130 ± 0.065) and a weakly positive dust-ACI index for the Middle configuration (0.080 ± 0.029), indicating a cloud brightening effect, where increases in DLOD are associated with decreases in R_e (see pink bars in Fig. 3a). In contrast, our results also show a slightly negative dust-ACI index for the Bottom configuration (−0.026 ± 0.021), indicating increases in DLOD are associated with increases in R_e (see pink bars in Fig. 3a). These relationships between dust and R_e vary with season for each configuration (red background in Fig. 3a). For the Top configuration, a negative dust-ACI index occurs only in spring (MAM), whereas the positive responses in the other three seasons dominate the mean positive dust-ACI index. For the Middle configuration, the mean positive dust-ACI index is mainly driven by the positive response in fall (SON), which compensates for the negative responses in winter (DJF) (Fig. 3a). Similarly, the mean negative dust-ACI index for the Bottom configuration is primarily dominated by the winter response, while the dust-ACI index remains close to zero in the other seasons (Fig. 3a). In addition to seasonal variations, the dust-ACI index across different dust–cloud configurations also depends on LWP (blue background in Fig. 3a). Specifically, we find that the dust-ACI index increases for higher LWP clouds for Top and Bottom configurations. Indeed, for the Bottom configuration, the dust-ACI index increases from negative for low-LWP clouds (20–60 g m^{-2}) to positive for high-LWP clouds (>100 g m^{-2}). For the Middle configuration, the dust-ACI index is highest for LWP in the range of 60–100 g m^{-2}, dominated by positive dust-ACI index in the summer and influenced by environmental factors (see Section 3.3 below).

These dust-ACI indices from ground-based instruments at ENA are further used to assess satellite-derived dust-ACI indices as a function of the dust–cloud configuration. We find that satellite-derived mean dust-ACI indices for Top and Middle configurations are largely consistent with those from ground-based instruments at ENA (except for Bottom), although with different magnitudes (Fig. 3a). Specifically, we find that the satellite-based mean dust-ACI indices are 0.013 ± 0.144 and 0.033 ± 0.316 for Top and Middle configurations, compared to 0.130 ± 0.065 and 0.080 ± 0.029 from ground-based

instruments. For the Bottom configuration, the results are opposite, showing 0.217 ± 0.140 for satellite-based dust-ACI relative to −0.026 ± 0.021 from ground-based observation. This difference in the sign of dust-ACI may reflect both sample size (see Fig. S4a) and differences in retrieval sensitivity and the representation of below-cloud dust layers between satellite and ground-based observations. Specifically, because satellite-retrieved R_e primarily represents cloud-top conditions, below-cloud dust is more difficult to compare directly with satellite-retrieved cloud microphysical properties (Platnick, 2000).

In contrast to the marine environment at ENA, we find different low-level cloud responses to DLOD at SGP (Fig. 3b). Because the Top category contains too few samples for a robust estimate, only the Middle and Bottom configurations are analyzed. We find that the mean dust-ACI indices are negative for the Middle configuration at SGP (−0.021 ± 0.057, positive for ENA) and positive for the Bottom configuration (0.086 ± 0.041, negative for ENA). These contrasting cloud responses to aerosols, such as dust, between marine and continental environments have also been documented in previous studies for non-dust aerosols (X. Ma et al., 2018) and attributed to differences in boundary layer coupling and thermodynamics, including surface fluxes, updraft differences between ocean and land (Su et al., 2024). In addition, the dust-ACI indices at SGP vary with season and LWP (Fig. 3b). Specifically, we find that the mean negative dust-ACI index for the Middle configuration is driven by negative responses in summer and fall, whereas the mean positive dust-ACI index for the Bottom configuration is driven by the positive responses in winter and spring. Across LWP regimes, the dust-ACI index changes from strongly positive for low-LWP clouds for both Middle and Bottom configurations to weak positive (Bottom) or negative (Middle) dust-ACI indices for high-LWP clouds, indicating an increase in R_e as LWP and associated available water vapor increase. Overall, the contrast between ENA and SGP suggests that dust impacts on cloud responses are jointly modulated by dust loading, vertical configuration, and environmental background, with marine and continental regimes favoring distinct cloud response patterns.

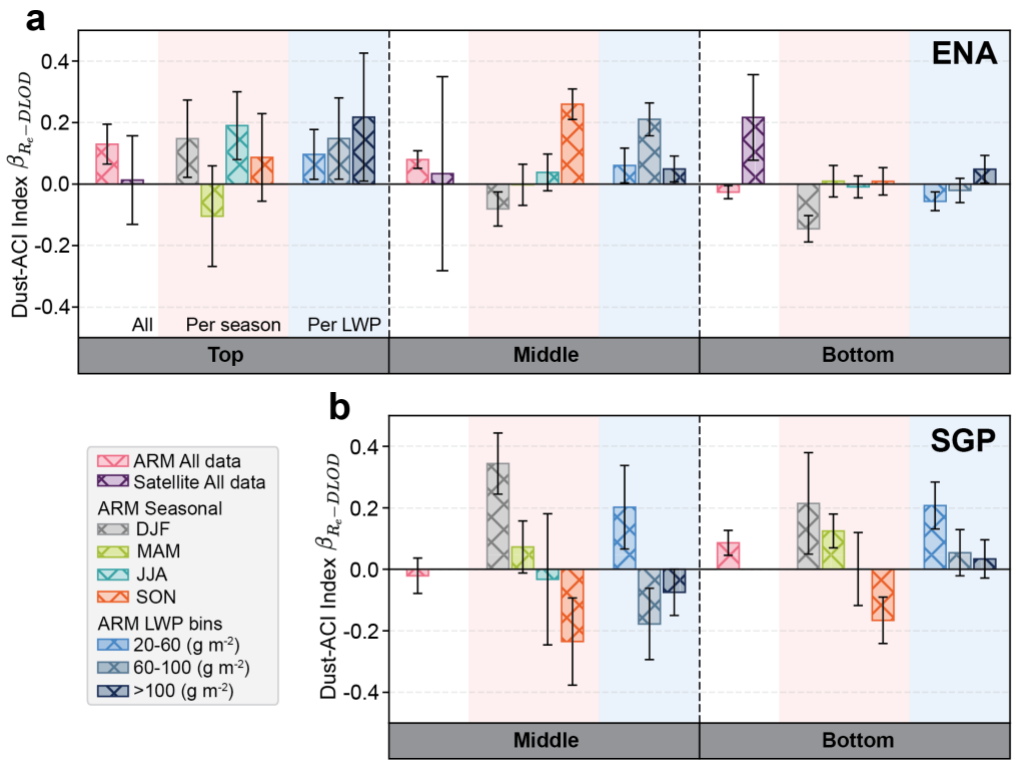

Figure 3. Cloud droplet radius sensitivity (β_{R_e-DLOD}) under different dust–cloud configurations (white background) and further stratified by season (red background) and LWP regimes (blue background) at (a) ENA and (b) SGP. Vertical lines denote the 95% confidence intervals.

3.3 Influence of Meteorology on Cloud Response to Dust–Cloud Configurations

To better understand the role of local meteorology on the low-level cloud responses, we break down the dust-ACI index as a function of common meteorological variables that influence low-level cloud development (Adebiyi & Zuidema, 2018). Although several meteorological variables influence cloud development differently over land and ocean (Ghonima et al., 2016; Jian et al., 2021; Klein et al., 2018), we limit our focus to five common variables ($RH_{750–850}$, $T_{750–850}$, LTS_{700}, $VWS_{725–925}$, and $VV_{750–850}$) to minimize multicollinearity arising from potential cross-correlations among them (see Text S2 and Fig. S2). For these five meteorological variables, we conduct a multiple linear regression analysis in which R_e is regressed on the variables and DLOD to minimize the confounding influence of meteorology on dust–cloud interactions (see Section 2.4). The results show that local meteorology substantially confounds estimates of the dust-ACI index, masking the direct microphysical responses of clouds to dust, the extent of which depends on dust–cloud configurations (Fig. 4). Specifically, the results show that the dust-ACI indices are largely positive after minimizing meteorological influence, suggesting that direct dust interactions often lead to decreases in R_e both over ocean and land. The highest dust-ACI index for ENA

remains for the Top configuration (0.092 ± 0.071), and the dust-ACI indices for the Bottom configuration are higher than those for the Middle configuration at both ENA and SGP (first column in Fig. 4a and 4c). At ENA, the dust-ACI index is 0.035 ± 0.031 for the Middle configuration and 0.029 ± 0.022 for the Bottom configuration; similarly, at SGP, it is 0.068 ± 0.067 for the Middle configuration and 0.190 ± 0.044 for the Bottom configuration. This difference in dust-ACI indices for direct dust interaction is associated with the competing microphysical and semi-direct influence of dust on R_e (see Fig. 5). When comparing the dust-ACI indices with and without the confounding influence of meteorology at ENA (Fig. 4a), we find that meteorological conditions tend to anomalously enhance dust–cloud interactions (decrease R_e) for Top and Middle configurations and suppress (increase R_e) dust–cloud interactions for Bottom configuration. At SGP, meteorological conditions anomalously suppress dust–cloud interactions in both the Middle and Bottom configurations, even changing the dust-ACI index from positive to negative for the Middle configuration.

In addition, the results show the relationship between each meteorological variable and cloud R_e, indicating their contributions to the anomalous enhancement or suppression of dust–cloud interactions. First, we find that an in-cloud increase in RH is associated with increases in R_e, except over land at SGP when dust is below the cloud (first column in Fig. 4b and 4d). Although increased R_e is expected for higher RH, it is likely that the advection of boundary-layer fine aerosols (including dust) over land into the cloud layer overcomes the increase in available moisture, resulting in a reduction in the cloud's R_e when dust is below cloud. Second, we find that an increase in in-cloud temperature is associated with a reduction in R_e, regardless of the dust–cloud configuration over ENA and SGP (second column in Fig. 4b and 4d). Such increases in in-cloud temperature can be caused by the shortwave absorption by dust particles heating the cloud layer (Koch & Del Genio, 2010; Kok et al., 2023), advection of warm free-tropospheric air entraining through the cloud top, or warm convective thermals increasing sensible heat flux from the surface, effectively raising the in-cloud temperature (Wood, 2012). Third, an increase in LTS is associated with increased cloud R_e over the ocean at ENA but reduced cloud R_e over land at SGP (third column in Fig. 4b and 4d). In both cases, the influence of LTS is stronger for the Top and Middle configurations than for the Bottom configurations. The strong LTS for the Top configuration is consistent with dust semi-direct effects when dust is above the cloud, resulting in moisture buildup in the boundary and cloud layer and an increase in R_e (Kok et al., 2023). In contrast, when dust is within or below clouds, other competing processes likely confound the effect of LTS, reducing its influence on cloud R_e. Fourth, we find that VWS has a contrasting influence on R_e at ENA and SGP (fourth column in Fig. 4b and 4d). Specifically, stronger VWS is associated with increased R_e for Middle configurations, although stronger

over land at SGP than over ocean at ENA. In contrast, R_e responds differently to stronger VWS for Bottom configurations, resulting in increased R_e at ENA and decreased R_e at SGP. Finally, our results also show that increases in upward vertical velocity reduce the cloud R_e, regardless of the dust–cloud configuration over ENA and SGP (last column in Fig. 4b and 4d). Overall, these results indicate that local meteorology modulates the dust-ACI index, indirectly influencing dust–cloud interaction, sometimes differently over ocean and land.

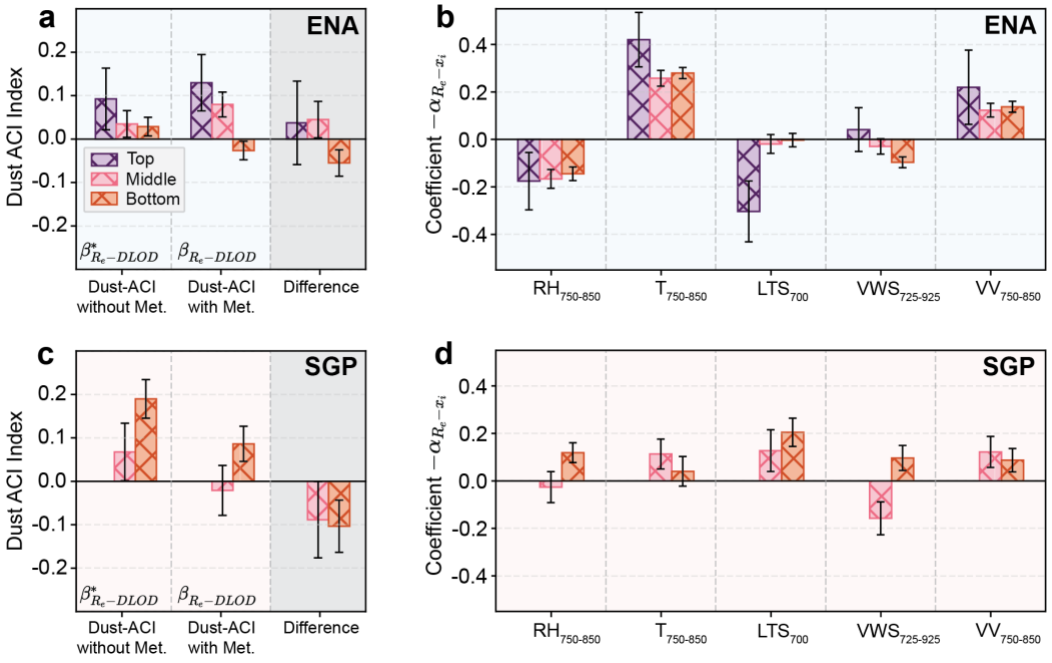

Figure 4. Confounding influence of meteorology on dust-cloud interactions under different dust–cloud vertical configurations. (a) Comparison of dust-ACI index estimated without meteorology ($\beta^*_{R_e-DLOD}$; minimizing the influence of meteorology), with meteorology (β_{R_e-DLOD} that is, the influence of meteorology remains), and their differences ($\beta_{R_e-DLOD} - \beta^*_{R_e-DLOD}$) in the ENA site under different dust–cloud configurations. (b) Standardized coefficients for meteorological variables ($-\alpha_{R_e-x_i}$) at the ENA site under different dust–cloud configurations. Note that the standardized coefficients for the meteorological variables are multiplied by -1 for comparison with the dust-ACI index (see Section 2.4). Panel (c) and (d) show the corresponding results for the SGP site. The figures are such that positive values indicate a decrease in cloud droplet effective radius with increasing predictor values. Vertical lines denote the 95% confidence intervals.

3.4 Potential Pathways Explaining Cloud Response to Dust-Cloud Configuration

Our findings above suggest that processes associated with dust–cloud interactions across different dust–cloud configurations are often more interconnected than can be explained by semi-direct (thermodynamic) or microphysical effects alone. Therefore, we propose the following pathways by which dust influences cloud droplet effective radius (R_e) across different dust-cloud configurations. First, when dust is above the cloud, the

dominant pathway influencing changes in R_e is likely the semi-direct effect, whereby dust-induced shortwave absorption warms the free troposphere (Wilcox, 2010), strengthens the lower-tropospheric stability (Johnson et al., 2004; Amiri-Farahani et al., 2017), suppresses cloud-top entrainment of dry air (Brioude et al., 2009), and traps moisture within the boundary layer (Fig. 5a; Kok et al., 2023). With less entrainment of dry air, the low-level cloud can maintain higher droplet number concentrations, which likely shifts the cloud droplet distribution toward smaller R_e for a comparable liquid water path (Twomey, 1977). In addition, enhanced shortwave-induced stability may also prolong cloud persistence, and thinner, shallower clouds with reduced turbulent mixing may more readily preserve high droplet number concentrations, further reducing R_e. In contrast to the shortwave warming above the cloud, the longwave-induced changes at cloud top, recently highlighted by Pandey and Adebiyi (2026a, 2026b), are likely small due to the observed low DLOD values (Fig. 2b and 2f), thereby limiting their impacts on Re. Furthermore, this pathway is supported by the strong response of R_e to LTS, VWS, and VV over ENA (Fig. 4b and 4d) as well as thinner clouds and lower cloud-top height (Fig. 2j). The net result is a reduction in R_e, consistent with the strong positive dust-ACI index observed at ENA for the Top configuration.

Second, when dust co-exists within the cloud layer, R_e is simultaneously influenced by competing microphysical and semi-direct pathways, making the net response strongly dependent on the ambient environment (Fig. 5b). On the one hand, dust can act as a conventional CCN (although with low hygroscopicity) (Karydis et al., 2011), increasing the droplet number concentration and shifting the size distribution toward smaller droplets, thereby reducing R_e (Karydis et al., 2017). On the other hand, dust absorption of shortwave radiation within the cloud can warm the layer and promote partial evaporation, which may either reduce or broaden the droplet spectrum depending on humidity and LWP. Over the ocean at ENA, where background CCN is low, the additional fine-mode dust CCN are comparatively more influential, yielding smaller R_e and a positive dust-ACI index. The supporting meteorology reinforces this cloud brightening pathway (Fig. 4b), whereby stronger upward vertical velocity enhances supersaturation that activates a larger number of CCN and yields more numerous smaller droplets, an effect that is especially pronounced in the updraft-sensitive (aerosol-limited) marine regime (Peng et al., 2005; Reutter et al., 2009). Over land at SGP, the already high background CCN concentration diminishes the marginal sensitivity of R_e to additional fine-mode dust, so the semi-direct warming-driven evaporation can dominate, sometimes leading to larger R_e and a negative dust-ACI index. This tendency is strengthened by meteorological conditions that promote droplet growth, including increased vertical wind shear (Fig. 4d), which enhances turbulent mixing and can deepen the cloud layer (Fig. 2j), both of which favor a larger cloud droplet effective radius.

Third, when dust is below the cloud layer, our result suggests that influence on R_e is likely governed by competing thermodynamic and microphysical pathways that diverge markedly between ocean and land (Fig. 5c). Sub-cloud radiative heating by dust warms the boundary layer, reduces sub-cloud relative humidity, elevates cloud base height, and modifies turbulent mixing (Koch & Del Genio, 2010; Kok et al., 2023), consistent with observed properties for Bottom configurations (Fig. 2j). Over ENA, weaker marine boundary-layer mixing and slower aerosol processing favor coarser dust acting as giant CCN at cloud

base, producing fewer but larger droplets that increase R_e, yielding a negative dust-ACI index, an effect amplified at low LWP (Fig. 3a). Additionally, shear-driven turbulent mixing within the boundary layer can help increase in-cloud water vapor, and consequently broaden the droplet spectrum, thereby increasing R_e resulting in a negative dust-ACI index (Fig. 4b). Over land at SGP, stronger convective boundary-layer mixing can exist, efficiently transporting finer, locally emitted dust particles upward to the cloud base, where they activate predominantly as conventional CCN, increasing droplet number concentration, reducing R_e, and producing a positive dust-ACI index, with high LWP weakening this sensitivity (Fig. 3b). Overall, these configuration-specific and environment-dependent mechanisms highlight that the sign and magnitude of dust effects on R_e emerge from a balance between semi-direct thermodynamic adjustments and microphysical pathways, which must be disentangled from meteorological confounding to isolate the true dust–cloud interaction.

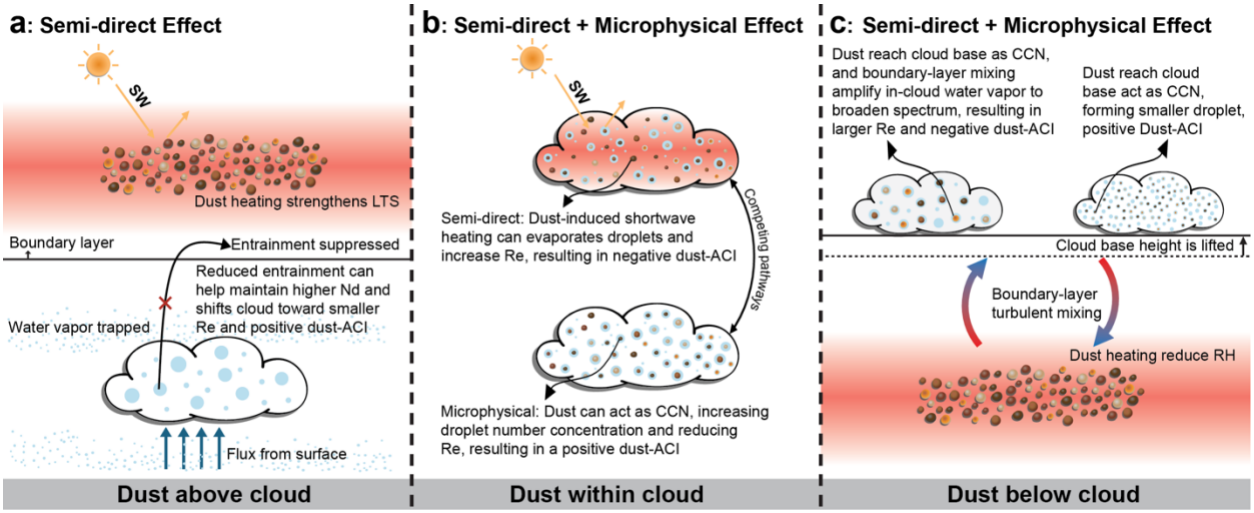

Figure 5. Schematic diagram of dust-ACI pathways under different vertical configurations. (a) Dust above cloud, where dust heating strengthens lower-tropospheric stability, suppresses entrainment, maintains cloud number concentration (Nd), and reduces cloud droplet effective radius (R_e); (b) Dust within cloud, where semi-direct evaporation and CCN activation compete to either increase or decrease R_e; and (c) dust below cloud, where sub-cloud heating and boundary-layer mixing regulate whether the R_e response is dominated by water-vapor influence that broadens droplet-spectrum, or conventional CCN activation that narrows it.

4 Discussion and Summary

Understanding how low-level clouds respond to mineral dust under different vertical configurations and meteorological conditions is critical for constraining aerosol–cloud interactions, an important component of regional climate systems. Using ground-based observations at the U.S. Department of Energy Atmospheric Radiation Measurement sites at the Eastern North Atlantic (ENA, marine) and the Southern Great Plains (SGP, continental), our analysis demonstrates that the response of low-level clouds to dust depends strongly on the relative vertical configuration between dust and cloud layers –

classified as dust above (Top), within (Middle), or below (Bottom) the cloud – and these responses differ substantially between marine and continental environments. Across both the ENA and SGP, ground-based lidar shows that the Bottom and Middle dust–cloud configurations occur substantially more frequently than the Top configuration. This low occurrence frequency of the Top configuration contrasts with satellite-based observations, which show higher occurrence rates than those of the Bottom configuration, highlighting the difficulty of observing dust above clouds for surface lidars (Griesche et al., 2024; Thorsen et al., 2011). Despite its relatively low occurrence frequency, the Top configuration at ENA exhibits the strongest positive dust-ACI index (log–log sensitivity of the cloud droplet effective radius to dust-layer optical depth), indicating cloud brightening through reductions in R_e with increasing DLOD, aided by local meteorology. In contrast, the Bottom and Middle configurations exhibit contrasting dust-ACI indices over ocean and land that are strongly modulated by LWP and local meteorological conditions. Specifically, over the marine site at ENA, local meteorology amplifies the positive dust-ACI index for the Middle configuration and suppresses it for the Bottom configuration. In addition, increased LWP in both configurations enhances the dust-ACI index, even resulting in positive values at the high-LWP regime for the Bottom configuration. Over the continental site at SGP, LWP and local meteorology suppress the dust-ACI indices for both the Middle and Bottom configurations, resulting in a negative dust-ACI index for the Middle configuration and a reduced positive dust-ACI index for the Bottom configuration.

These contrasting cloud responses can be understood through three pathways that balance semi-direct and microphysical effects (Fig. 5). For the Top configuration, shortwave absorption warms the overlying free troposphere and strengthens lower-tropospheric stability, suppressing cloud-top entrainment of dry air and preserving higher droplet number concentrations in the resulting thinner, shallower clouds, thereby reducing R_e and producing the strong positive dust-ACI index at ENA. For the Middle configuration, competing pathways dominate in different regimes, whereby over the marine ENA, where background CCN are scarce, fine-mode dust activates additional droplets and reduces R_e, whereas over the continental SGP, abundant background CCN mute this effect while in-cloud absorptive warming evaporates droplets and increases R_e . For the Bottom configuration, sub-cloud heating elevates the cloud base, and the dominant nucleating mode diverges between environments: coarse dust can act as giant CCN over the weakly mixed marine boundary layer aided by increased in-cloud water vapor, forming fewer, larger droplets, while strong continental mixing delivers finer dust that activates as conventional CCN, reducing R_e. Across all three configurations, local meteorology modulates dust-cloud sensitivities, masking an underlying microphysical brightening that emerges once meteorological covariability is removed.

Our findings have important implications for the assessment of dust–cloud interactions in climate models. Current climate and regional models typically represent aerosol–cloud interactions using column-integrated aerosol optical depth or near-surface aerosol concentration as proxies for the aerosol burden that influences clouds (P.-L. Ma et al., 2018; Painemal et al., 2020). Our results demonstrate that such column-integrated metrics are insufficient to capture the configuration-dependent cloud responses

documented here, because the sign and magnitude of the dust-ACI index depend not only on dust loading but critically on where dust resides relative to the cloud layer (Fig. 3 and 4). In addition, this problem is compounded by the well-documented difficulty that climate models have in accurately simulating dust vertical distributions, particularly the elevated transport of coarse dust that characterizes long-range pathways to sites such as ENA (Adebiyi et al., 2023; O'Sullivan et al., 2020). Furthermore, our results highlight that the environmental regime (marine or continental) influences the microphysical and semi-direct (thermodynamic) pathways through which dust affects R_e, because this determines whether meteorology enhances or suppresses dust–cloud interactions (Fig. 4).

Our findings are subject to some caveats. First, an important limitation of our study is the low occurrence frequency of the Top dust–cloud configuration at both ARM sites, particularly at SGP, where it is too rare for robust statistical analysis. This limitation arises partly from the physical rarity of elevated dust above low-level clouds at these locations, but also from an inherent constraint of ground-based lidar. Specifically, signal attenuation by the intervening cloud layer reduces sensitivity to aerosol layers residing above clouds, increasing retrieval uncertainty for the Top configuration relative to the Bottom configuration (Proestakis et al., 2018; Thorsen et al., 2017). This asymmetry is the inverse of the attenuation challenge faced by spaceborne lidars such as CALIPSO, for which cloud attenuation preferentially limits detection of below-cloud dust and therefore under-sample the Bottom configuration (Fig. 2a and Fig. S4a). One approach for future studies to minimize this limitation is to perform coordinated aircraft-based in situ measurements during dust transport events, which could provide direct characterization of above-cloud dust properties that are inaccessible to passive or attenuated lidar retrievals (Cochrane et al., 2019; Wang et al., 2022). Second, another key limitation is that the median DLOD at both ENA and SGP is very low (Fig. 2b and 2f), reflecting their position off the major dust-transport corridors (Wang et al., 2020; Lambert et al., 2020). At such low loadings, the dust-induced perturbation to cloud droplet effective radius is small and difficult to separate from meteorological covariability, limiting statistical power and the generalizability of the inferred sensitivities. As such, our observed sensitivities likely represent the lower bound of dust–cloud interactions (Kok et al., 2023). Importantly, the balance between semi-direct and microphysical pathways is likely nonlinear; under high-DLOD conditions, stronger shortwave absorption could amplify semi-direct or thermodynamic adjustments relative to microphysical effects (Pandey et al., 2026c), potentially altering the sign and magnitude of the dust-ACI index reported here. Third, although our multiple linear regression controls for five meteorological variables, it cannot fully isolate the dust signal, because dust-induced semi-direct heating is itself embedded within the thermodynamic background (Johnson et al., 2004). Consequently, the meteorology-adjusted dust-ACI index likely reflects statistical covariability rather than a fully causal attribution of cloud responses to dust (Su et al., 2024). Regardless of these observational and methodological limitations, our findings indicate that future estimates of dust radiative forcing will depend critically on how well models and observations represent dust–cloud vertical configuration, because this configuration determines whether dust brightens or darkens low-level clouds through changes in cloud droplet effective radius and associated cloud albedo.

Acknowledgments

AAA acknowledges support from the U.S. Department of Energy (DOE), Office of Science (award DE-SC0024281).

Open Research

The processed data and analysis code used to reproduce the results in this study are available through Zenodo at https://zenodo.org/records/20696213. The original observational data used in this study were obtained from publicly available data repositories. CALIPSO fine- and coarse-mode dust products developed by Proestakis et al. (2024) are available at https://zenodo.org/records/10389741. CloudSat observations are available from the CloudSat Data Processing Center at https://www.cloudsat.cira.colostate.edu/. MODIS data were obtained from the A-Train Data Depot at NASA GES DISC at https://atrain.gesdisc.eosdis.nasa.gov/data/MAC/MAC06S0.002/. ARM observations were obtained from the U.S. Department of Energy Atmospheric Radiation Measurement Data Center, including RLPROF-FEX for aerosol extinction, depolarization ratio, and scattering ratio at https://www.arm.gov/data/science-data-products/vaps/rlprof-fex; ARSCL for cloud base height, cloud top height, and cloud-layer information at https://www.arm.gov/data/science-data-products/vaps/arscl; MFRSRCLDOD for cloud droplet effective radius and liquid water path at https://www.arm.gov/data/science-data-products/vaps/mfrsrcldod; SONDEGRID for relative humidity, temperature, potential temperature, and wind speed at https://www.arm.gov/data/science-data-products/vaps/sondegrid; and DLPROF-WSTATS for Doppler-lidar vertical velocity statistics at https://www.arm.gov/data/science-data-products/vaps/dlprof-wstats.

Conflict of Interest

The authors declare there are no conflicts of interest for this study.

References

Adebiyi, A. A., & Kok, J. F. (2020). Climate models miss most of the coarse dust in the atmosphere. *Science Advances*, 6(15), eaaz9507. https://doi.org/10.1126/sciadv.aaz9507

Adebiyi, A. A., & Zuidema, P. (2018). Low cloud cover sensitivity to biomass-burning aerosols and meteorology over the southeast Atlantic. *Journal of Climate*, 31(11), 4329–4346. https://doi.org/10.1175/JCLI-D-17-0406.1

Adebiyi, A. A., Kok, J. F., Murray, B. J., Ryder, C. L., Stuut, J.-B. W., Kahn, R. A., Knippertz, P., Formenti, P., Mahowald, N. M., & García-Pando, C. P. (2023). A review of coarse mineral dust in the Earth system. *Aeolian Research*, 60, 100849. https://doi.org/10.1016/j.aeolia.2022.100849

Adebiyi, A. A., Zuidema, P., & Abel, S. J. (2015). The convolution of dynamics and moisture with the presence of shortwave absorbing aerosols over the southeast Atlantic. *Journal of Climate,* 28(5), 1997–2024. https://doi.org/10.1175/JCLI-D-14-00352.1

Amiri-Farahani, A., Allen, R. J., Neubauer, D., & Lohmann, U. (2017). Impact of Saharan dust on North Atlantic marine stratocumulus clouds: Importance of the semidirect effect. *Atmospheric Chemistry and Physics*, 17(10), 6305–6322. https://doi.org/10.5194/acp-17-6305-2017

Behrendt, A., & Nakamura, T. (2002). Calculation of the calibration constant of polarization lidar and its dependency on atmospheric temperature. *Optics Express*, 10(16), 805–817. https://doi.org/10.1364/OE.10.000805

Bellouin, N., Quaas, J., Gryspeerdt, E., Kinne, S., Stier, P., Watson-Parris, D., Boucher, O., Carslaw, K. S., Christensen, M., & Daniau, A. (2020). Bounding global aerosol radiative forcing of climate change. *Reviews of Geophysics*, 58(1), e2019RG000660. https://doi.org/10.1029/2019RG000660

Bender, F. A. (2020). Aerosol forcing: Still uncertain, still relevant. *AGU Advances*, 1(3), e2019AV000128. https://doi.org/10.1029/2019AV000128

Brioude, J., Cooper, O. R., Feingold, G., Trainer, M., Freitas, S. R., Kowal, D., Ayers, J. K., Prins, E., Minnis, P., McKeen, S. A., Frost, G. J., Hsie, E. Y., & Weinheimer, A. J. (2009). Effect of biomass burning on marine stratocumulus clouds off the California coast. *Atmospheric Chemistry and Physics*, 9(22), 8841–8856. https://doi.org/10.5194/acp-9-8841-2009

Burton, S. P., Hair, J. W., Kahnert, M., Ferrare, R. A., Hostetler, C. A., Cook, A. L., Harper, D. B., Berkoff, T. A., Seaman, S. T., & Collins, J. E. (2015). Observations of the spectral dependence of linear particle depolarization ratio of aerosols using NASA Langley airborne High Spectral Resolution Lidar. *Atmospheric Chemistry and Physics*, 15(23), 13453–13473. https://doi.org/10.5194/acp-15-13453-2015

Chand, D., Newsom, R., Thorsen, T., Cromwell, E., Sivaraman, C., Flynn, C., Shilling, J., & Comstock, J. M. (2023). Aerosol and Cloud Optical Properties from the ARM Raman Lidars: The Feature Detection and Extinction (FEX) Value-Added Product. U.S. Department of Energy, *Atmospheric Radiation Measurement user facility*, Richland, Washington. DOE/SC-ARM-TR224.

Chen, R., Wood, R., Li, Z., Ferraro, R., & Chang, F. (2008). Studying the vertical variation of cloud droplet effective radius using ship and space-borne remote sensing data.

Journal of Geophysical Research: Atmospheres, 113(D8), D00A02. https://doi.org/10.1029/2007JD009596

Clothiaux, E. E., Miller, M. A., Perez, R. C., Turner, D. D., Moran, K. P., Martner, B. E., Ackerman, T. P., Mace, G. G., Marchand, R. T., Widener, K. B., Rodriguez, D. J., Uttal, T., Mather, J. H., Flynn, C. J., Gaustad, K. L., & Ermold, B. (2001). The ARM millimeter wave cloud radars (MMCRs) and the active remote sensing of clouds (ARSCL) value added product (VAP). DOE Technical Memorandum, ARM VAP-002.1. U.S. Department of Energy, Office of Science, *Atmospheric Radiation Measurement Program*. https://doi.org/10.2172/1808567

Cochrane, S. P., Schmidt, K. S., Chen, H., Pilewskie, P., Kittelman, S., Redemann, J., LeBlanc, S., Pistone, K., Kacenelenbogen, M., & Segal Rozenhaimer, M. (2019). Above-cloud aerosol radiative effects based on ORACLES 2016 and ORACLES 2017 aircraft experiments. *Atmospheric Measurement Techniques*, 12(12), 6505–6528. https://doi.org/10.5194/amt-12-6505-2019

Evans, S. (2025). Dust-producing weather patterns of the North American Great Plains. *Atmospheric Chemistry and Physics*, 25(9), 4833–4845. https://doi.org/10.5194/acp-25-4833-2025

Fairless, T., Jensen, M., Zhou, A., & Giangrande, S. E. (2021). Interpolated Sounding and Gridded Sounding Value-Added Products. U.S. Department of Energy, Office of Science, *Atmospheric Radiation Measurement Program*. https://doi.org/10.2172/1248938

Fan, J., Yuan, T., Comstock, J. M., Ghan, S., Khain, A., Leung, L. R., Li, Z., Martins, V. J., & Ovchinnikov, M. (2009). Dominant role by vertical wind shear in regulating aerosol effects on deep convective clouds. *Journal of Geophysical Research: Atmospheres*, 114(D22), D22206. https://doi.org/10.1029/2009JD012352

Freudenthaler, V., Esselborn, M., Wiegner, M., Heese, B., Tesche, M., Ansmann, A., Müller, D., Althausen, D., Wirth, M., & Fix, A. (2009). Depolarization ratio profiling at several wavelengths in pure Saharan dust during SAMUM 2006. *Tellus B: Chemical and Physical Meteorology*, 61(1), 165–179. https://doi.org/10.1111/j.1600-0889.2008.00396.x

Ghonima, M. S., Heus, T., Norris, J. R., & Kleissl, J. (2016). Factors controlling stratocumulus cloud lifetime over coastal land. *Journal of the Atmospheric Sciences*, 73(8), 2961–2983. https://doi.org/10.1175/JAS-D-15-0325.1

Griesche, H. J., Seifert, P., Engelmann, R., Radenz, M., Hofer, J., Althausen, D., Walbröl, A., Barrientos-Velasco, C., Baars, H., Dahlke, S., Tukiainen, S., & Macke, A. (2024). Cloud micro- and macrophysical properties from ground-based remote sensing during the MOSAiC drift experiment. *Scientific Data*, 11(1), 505. https://doi.org/10.1038/s41597-024-03325-w

Haarig, M., Ansmann, A., Engelmann, R., Baars, H., Toledano, C., Torres, B., Althausen, D., Radenz, M., & Wandinger, U. (2022). First triple-wavelength lidar observations of depolarization and extinction-to-backscatter ratios of Saharan dust. *Atmospheric Chemistry and Physics*, 22(1), 355–369. https://doi.org/10.5194/acp-22-355-2022

Hong, Y., & Di Girolamo, L. (2022). An overview of aerosol properties in clear and cloudy sky based on CALIPSO observations. *Earth and Space Science*, 9(4), e2022EA002287. https://doi.org/10.1029/2022EA002287

Huang, C.-C., Chen, S.-H., Lin, Y.-C., Earl, K., Matsui, T., Lee, H.-H., Tsai, I.-C., Chen, J.-P., & Cheng, C.-T. (2019). Impacts of dust-radiation versus dust-cloud interactions on the development of a modeled mesoscale convective system over North Africa. *Monthly Weather Review*, 147(9), 3301–3326. https://doi.org/10.1175/MWR-D-18-0459.1

Im, U., Samset, B. H., Nenes, A., Thomas, J. L., Kokkola, H., Dubovik, O., Amiridis, V., Arola, A., Bellouin, N., & Benedetti, A. (2026). Aerosol-cloud interactions: Overcoming a barrier to projecting near-term climate evolution and risk. *AGU Advances*, 7(1), e2025AV001872. https://doi.org/10.1029/2025AV001872

Jia, H., Ma, X., Quaas, J., Yin, Y., & Qiu, T. (2019). Is positive correlation between cloud droplet effective radius and aerosol optical depth over land due to retrieval artifacts or real physical processes? *Atmospheric Chemistry and Physics*, 19(13), 8879–8896. https://doi.org/10.5194/acp-19-8879-2019

Jia, H., Ma, X., Yu, F., & Quaas, J. (2021). Significant underestimation of radiative forcing by aerosol-cloud interactions derived from satellite-based methods. *Nature Communications*, 12(1), 3649. https://doi.org/10.1038/s41467-021-23888-1

Jian, B., Li, J., Wang, G., Zhao, Y., Li, Y., Wang, J., Zhang, M., & Huang, J. (2021). Evaluation of the CMIP6 marine subtropical stratocumulus cloud albedo and its controlling factors. *Atmospheric Chemistry and Physics*, 21(12), 9809–9828. https://doi.org/10.5194/acp-21-9809-2021

Johnson, B. T., Shine, K. P., & Forster, P. M. (2004). The semi-direct aerosol effect: Impact of absorbing aerosols on marine stratocumulus. *Quarterly Journal of the Royal Meteorological Society*, 130(599), 1407–1422. https://doi.org/10.1256/qj.03.61

Kacenelenbogen, M., Redemann, J., Vaughan, M. A., Omar, A. H., Russell, P. B., Burton, S., Rogers, R. R., Ferrare, R. A., & Hostetler, C. A. (2014). An evaluation of CALIOP/CALIPSO's aerosol-above-cloud detection and retrieval capability over North America. *Journal of Geophysical Research: Atmospheres*, 119(1), 230–244. https://doi.org/10.1002/2013JD020178

Karydis, V. A., Kumar, P., Barahona, D., Sokolik, I. N., & Nenes, A. (2011). On the effect of dust particles on global cloud condensation nuclei and cloud droplet number. *Journal of Geophysical Research: Atmospheres,* 116(D23), D23204. https://doi.org/10.1029/2011JD016283

Karydis, V. A., Tsimpidi, A. P., Bacer, S., Pozzer, A., Nenes, A., & Lelieveld, J. (2017). Global impact of mineral dust on cloud droplet number concentration. *Atmospheric Chemistry and Physics*, 17(9), 5601–5621. https://doi.org/10.5194/acp-17-5601-2017

Kim, D., Chin, M., Yu, H., Diehl, T., Tan, Q., Kahn, R. A., Tsigaridis, K., Bauer, S. E., Takemura, T., Pozzoli, L., Bellouin, N., Schulz, M., Peyridieu, S., Chédin, A., & Koffi, B. (2014). Sources, sinks, and transatlantic transport of North African dust aerosol: A multimodel analysis and comparison with remote sensing data. *Journal of Geophysical Research: Atmospheres*, 119(10), 6259–6277. https://doi.org/10.1002/2013JD021099

Kim, S.-W., Berthier, S., Raut, J.-C., Chazette, P., Dulac, F., & Yoon, S.-C. (2008). Validation of aerosol and cloud layer structures from the space-borne lidar CALIOP using a ground-based lidar in Seoul, Korea. *Atmospheric Chemistry and Physics*, 8(13), 3705–3720. https://doi.org/10.5194/acp-8-3705-2008

Klein, S. A., Hall, A., Norris, J. R., & Pincus, R. (2018). Low-cloud feedbacks from cloud-controlling factors: A review. *Shallow Clouds, Water Vapor, Circulation, and Climate Sensitivity*, 135–157. https://doi.org/10.1007/s10712-017-9433-3

Koch, D., & Del Genio, A. D. (2010). Black carbon semi-direct effects on cloud cover: Review and synthesis. *Atmospheric Chemistry and Physics*, 10(16), 7685–7696. https://doi.org/10.5194/acp-10-7685-2010

Kok, J. F., Adebiyi, A. A., Albani, S., Balkanski, Y., Checa-Garcia, R., Chin, M., Colarco, P. R., Hamilton, D. S., Huang, Y., Ito, A., Klose, M., Li, L., Mahowald, N. M., Miller, R. L., Obiso, V., Pérez García-Pando, C., Rocha-Lima, A., & Wan, J. S. (2021). Contribution of the world's main dust source regions to the global cycle of desert dust. *Atmospheric Chemistry and Physics*, 21(10), 8169–8193. https://doi.org/10.5194/acp-21-8169-2021

Kok, J. F., Storelvmo, T., Karydis, V. A., Adebiyi, A. A., Mahowald, N. M., Evan, A. T., He, C., & Leung, D. M. (2023). Mineral dust aerosol impacts on global climate and climate change. *Nature Reviews Earth & Environment*, 4(2), 71–86. https://doi.org/10.1038/s43017-022-00379-5

Lambert, A., Hallar, A. G., Garcia, M., Strong, C., Andrews, E., & Hand, J. L. (2020). Dust impacts of rapid agricultural expansion on the Great Plains. *Geophysical Research Letters*, 47(20), e2020GL090347. https://doi.org/10.1029/2020GL090347

Li, J., Carlson, B. E., Yung, Y. L., Lv, D., Hansen, J., Penner, J. E., Liao, H., Ramaswamy, V., Kahn, R. A., & Zhang, P. (2022). Scattering and absorbing aerosols in the climate system. *Nature Reviews Earth & Environment*, 3(6), 363–379. https://doi.org/10.1038/s43017-022-00296-7

Lin, Y., Takano, Y., Gu, Y., Wang, Y., Zhou, S., Zhang, T., Zhu, K., Wang, J., Zhao, B., & Chen, G. (2023). Characterization of the aerosol vertical distributions and their impacts on warm clouds based on multi-year ARM observations. *Science of The Total Environment*, 904, 166582. https://doi.org/10.1016/j.scitotenv.2023.166582

Liu, Z., Vaughan, M., Winker, D., Kittaka, C., Getzewich, B., Kuehn, R., Omar, A., Powell, K., Trepte, C., & Hostetler, C. (2009). The CALIPSO lidar cloud and aerosol discrimination: Version 2 algorithm and initial assessment of performance. *Journal of Atmospheric and Oceanic Technology*, 26(7), 1198–1213. https://doi.org/10.1175/2009JTECHA1229.1

Lohmann, U., & Lesins, G. (2003). Comparing continental and oceanic cloud susceptibilities to aerosols. *Geophysical Research Letters*, 30(15), 1791. https://doi.org/10.1029/2003GL017828

Ma, P.-L., Rasch, P. J., Chepfer, H., Winker, D. M., & Ghan, S. J. (2018). Observational constraint on cloud susceptibility weakened by aerosol retrieval limitations. *Nature Communications*, 9(1), 2640. https://doi.org/10.1038/s41467-018-05028-4

Ma, X., Jia, H., Yu, F., & Quaas, J. (2018). Opposite aerosol index-cloud droplet effective radius correlations over major industrial regions and their adjacent oceans. *Geophysical Research Letters*, 45(11), 5771–5778. https://doi.org/10.1029/2018GL077562

Mamouri, R.-E., & Ansmann, A. (2014). Fine and coarse dust separation with polarization lidar. *Atmospheric Measurement Techniques*, 7(11), 3717–3735. https://doi.org/10.5194/amt-7-3717-2014

Mann, J. A. L., Chiu, J. C., Hogan, R. J., O'Connor, E. J., L'Ecuyer, T. S., Stein, T. H. M., & Jefferson, A. (2014). Aerosol impacts on drizzle properties in warm clouds from ARM Mobile Facility maritime and continental deployments. *Journal of Geophysical Research: Atmospheres*, 119(7), 4136–4148. https://doi.org/10.1002/2013JD021339

Martins, J. V., Marshak, A., Remer, L. A., Rosenfeld, D., Kaufman, Y. J., Fernandez-Borda, R., Koren, I., Correia, A. L., Zubko, V., & Artaxo, P. (2011). Remote sensing the vertical profile of cloud droplet effective radius, thermodynamic phase, and temperature. *Atmospheric Chemistry and Physics*, 11(18), 9485–9501. https://doi.org/10.5194/acp-11-9485-2011

McFarquhar, G. M., & Wang, H. (2006). Effects of aerosols on trade wind cumuli over the Indian Ocean: Model simulations. *Quarterly Journal of the Royal Meteorological Society*, 132(616), 821–843. https://doi.org/10.1256/qj.04.179

McHardy, T. M., Dong, X., Xi, B., Thieman, M. M., Minnis, P., & Palikonda, R. (2018). Comparison of daytime low-level cloud properties derived from GOES and ARM SGP measurements. *Journal of Geophysical Research: Atmospheres*, 123(15), 8221–8237. https://doi.org/10.1029/2018JD028911

Newsom, R. K., Bambha, R., & Chand, D. (2022). Raman Lidar (RL) Instrument Handbook. U.S. Department of Energy, *Atmospheric Radiation Measurement User Facility*. https://doi.org/10.2172/1020561

Noh, Y., Müller, D., Lee, K., Kim, K., Lee, K., Shimizu, A., Sano, I., & Park, C. B. (2017). Depolarization ratios retrieved by AERONET sun-sky radiometer data and comparison to depolarization ratios measured with lidar. *Atmospheric Chemistry and Physics*, 17(10), 6271–6290. https://doi.org/10.5194/acp-17-6271-2017

O'Sullivan, D., Marenco, F., Ryder, C. L., Pradhan, Y., Kipling, Z., Johnson, B., Benedetti, A., Brooks, M., McGill, M., & Yorks, J. (2020). Models transport Saharan dust too low in the atmosphere: A comparison of the MetUM and CAMS forecasts with observations. *Atmospheric Chemistry and Physics*, 20(21), 12955–12982. https://doi.org/10.5194/acp-20-12955-2020

Painemal, D., Chang, F.-L., Ferrare, R., Burton, S., Li, Z., Smith, W. L., Jr., Minnis, P., Feng, Y., & Clayton, M. (2020). Reducing uncertainties in satellite estimates of aerosol-cloud interactions over the subtropical ocean by integrating vertically resolved aerosol observations. *Atmospheric Chemistry and Physics*, 20(12), 7167–7177. https://doi.org/10.5194/acp-20-7167-2020

Pandey, S. K., & Adebiyi, A. A. (2026a). Dust and smoke layers over the Atlantic Ocean weaken the underlying low-level cloud-top radiative cooling through different pathways. *Communications Earth & Environment*, 7, 160. https://doi.org/10.1038/s43247-026-03183-x

Pandey, S. K., & Adebiyi, A. A. (2026b). Dust semi-direct effects: Low-level cloud response to free-tropospheric dust-induced longwave radiation over the North Atlantic Ocean. *Atmospheric Chemistry and Physics*, 26(1), 217–246. https://doi.org/10.5194/acp-26-217-2026

Pandey, S. K., Adebiyi, A. A., Lian, Y., Vinoj, V., & Zheng, X. (2026c). Dust suppresses aerosol first indirect effects in marine warm clouds over the North Atlantic Ocean. *Communications Earth & Environment*. https://doi.org/10.1038/s43247-026-03693-8

Patnaude, R., & Diao, M. (2020). Aerosol indirect effects on cirrus clouds based on global aircraft observations. *Geophysical Research Letters*, 47(10), e2019GL086550. https://doi.org/10.1029/2019GL086550

Peng, Y., Lohmann, U., & Leaitch, R. (2005). Importance of vertical velocity variations in the cloud droplet nucleation process of marine stratus clouds. *Journal of Geophysical Research: Atmospheres*, 110(D21), D21213. https://doi.org/10.1029/2004JD004922

Platnick, S. (2000). Vertical photon transport in cloud remote sensing problems. *Journal of Geophysical Research: Atmospheres*, 105(D18), 22919–22935. https://doi.org/10.1029/2000JD900333

Proestakis, E., Amiridis, V., Marinou, E., Georgoulias, A. K., Solomos, S., Kazadzis, S., Chimot, J., Che, H., Alexandri, G., & Binietoglou, I. (2018). Nine-year spatial and temporal evolution of desert dust aerosols over South and East Asia as revealed by CALIOP. *Atmospheric Chemistry and Physics*, 18(2), 1337–1362. https://doi.org/10.5194/acp-18-1337-2018

Proestakis, E., Gkikas, A., Georgiou, T., Kampouri, A., Drakaki, E., Ryder, C. L., Marenco, F., Marinou, E., & Amiridis, V. (2024). A near-global multiyear climate data record of the fine-mode and coarse-mode components of atmospheric pure dust. *Atmospheric Measurement Techniques*, 17(12), 3625–3667. https://doi.org/10.5194/amt-17-3625-2024

Qiu, S., Zheng, X., Painemal, D., Terai, C. R., & Zhou, X. (2024). Daytime variation in the aerosol indirect effect for warm marine boundary layer clouds in the eastern North Atlantic. *Atmospheric Chemistry and Physics*, 24(5), 2913–2935. https://doi.org/10.5194/acp-24-2913-2024

Reutter, P., Su, H., Trentmann, J., Simmel, M., Rose, D., Gunthe, S. S., Wernli, H., Andreae, M. O., & Pöschl, U. (2009). Aerosol- and updraft-limited regimes of cloud droplet formation: Influence of particle number, size, and hygroscopicity on the activation of cloud condensation nuclei (CCN). *Atmospheric Chemistry and Physics*, 9(18), 7067–7080. https://doi.org/10.5194/acp-9-7067-2009

Sand, M., Samset, B. H., Myhre, G., Gliß, J., Bauer, S. E., Bian, H., Chin, M., Checa-Garcia, R., Ginoux, P., & Kipling, Z. (2021). Aerosol absorption in global models from AeroCom phase III. *Atmospheric Chemistry and Physics*, 21(20), 15929–15947. https://doi.org/10.5194/acp-21-15929-2021

Song, Q., Zhang, Z., Yu, H., Kato, S., Yang, P., Colarco, P., Remer, L. A., & Ryder, C. L. (2018). Net radiative effects of dust in the tropical North Atlantic based on integrated satellite observations and in situ measurements. *Atmospheric Chemistry and Physics*, 18(15), 11303–11322. https://doi.org/10.5194/acp-18-11303-2018

Soupiona, O., Papayannis, A., Kokkalis, P., Foskinis, R., Sánchez Hernández, G., Ortiz-Amezcua, P., Mylonaki, M., Papanikolaou, C.-A., Papagiannopoulos, N., & Samaras, S. (2020). EARLINET observations of Saharan dust intrusions over the northern Mediterranean region (2014–2017): Properties and impact on radiative forcing. *Atmospheric Chemistry and Physics*, 20(23), 15147–15166. https://doi.org/10.5194/acp-20-15147-2020

Su, T., Li, Z., Henao, N. R., Luan, Q., & Yu, F. (2024). Constraining effects of aerosol-cloud interaction by accounting for coupling between cloud and land surface. *Science Advances*, 10(21), eadl5044. https://doi.org/10.1126/sciadv.adl5044

Thorsen, T. J., Ferrare, R. A., Hostetler, C. A., Vaughan, M. A., & Fu, Q. (2017). The impact of lidar detection sensitivity on assessing aerosol direct radiative effects. *Geophysical Research Letters*, 44(17), 9059–9067. https://doi.org/10.1002/2017GL074521

Thorsen, T. J., Fu, Q., & Comstock, J. (2011). Comparison of the CALIPSO satellite and ground-based observations of cirrus clouds at the ARM TWP sites. *Journal of Geophysical Research: Atmospheres*, 116(D21), D21203. https://doi.org/10.1029/2011JD015970

Thorsen, T. J., Fu, Q., Newsom, R. K., Turner, D. D., & Comstock, J. M. (2015). Automated retrieval of cloud and aerosol properties from the ARM Raman lidar. Part I: Feature detection. *Journal of Atmospheric and Oceanic Technology*, 32(11), 1977–1998. https://doi.org/10.1175/JTECH-D-14-00150.1

Turner, D. D., McFarlane, S. A., Riihimaki, L., Shi, Y., Lo, C., & Min, Q. (2014). Cloud Optical Properties from the Multifilter Shadowband Radiometer (MFRSRCLDOD): An ARM Value-Added Product. U.S. Department of Energy, *Atmospheric Radiation Measurement Climate Research Facility*. DOE/SC-ARM-TR-139.

Twomey, S. (1977). The influence of pollution on the shortwave albedo of clouds. *Journal of the Atmospheric Sciences*, 34(7), 1149–1152. https://doi.org/10.1175/1520-0469(1977)034%3C1149:TIOPOT%3E2.0.CO;2

Voigt, A., Albern, N., Ceppi, P., Grise, K., Li, Y., & Medeiros, B. (2021). Clouds, radiation, and atmospheric circulation in the present-day climate and under climate change. *Wiley Interdisciplinary Reviews: Climate Change*, 12(2), e694. https://doi.org/10.1002/wcc.694

Wall, C. J., Norris, J. R., Possner, A., McCoy, D. T., McCoy, I. L., & Lutsko, N. J. (2022). Assessing effective radiative forcing from aerosol-cloud interactions over the global ocean. *Proceedings of the National Academy of Sciences*, 119(46), e2210481119. https://doi.org/10.1073/pnas.2210481119

Wang, J., Wood, R., Jensen, M. P., Chiu, J. C., Liu, Y., Lamer, K., Desai, N., Giangrande, S. E., Knopf, D. A., & Kollias, P. (2022). Aerosol and cloud experiments in the Eastern North Atlantic (ACE-ENA). *Bulletin of the American Meteorological Society*, 103(2), E619–E641. https://doi.org/10.1175/BAMS-D-19-0220.1

Wang, Y., Zheng, X., Dong, X., Xi, B., Wu, P., Logan, T., & Yung, Y. L. (2020). Impacts of long-range transport of aerosols on marine-boundary-layer clouds in the eastern North Atlantic. *Atmospheric Chemistry and Physics*, 20(23), 14741–14755. https://doi.org/10.5194/acp-20-14741-2020

Wang, Z., Yuan, J., Wood, R., Chen, Y., & Tong, T. (2023). Profile-based estimated inversion strength. *Atmospheric Chemistry and Physics*, 23(5), 3247–3266. https://doi.org/10.5194/acp-23-3247-2023

Watson-Parris, D., & Smith, C. J. (2022). Large uncertainty in future warming due to aerosol forcing. *Nature Climate Change*, 12(12), 1111–1113. https://doi.org/10.1038/s41558-022-01516-0

Wilcox, E. M. (2010). Stratocumulus cloud thickening beneath layers of absorbing smoke aerosol. *Atmospheric Chemistry and Physics*, 10(23), 11769–11777. https://doi.org/10.5194/acp-10-11769-2010

Wood, R. (2012). Stratocumulus clouds. *Monthly Weather Review*, 140(8), 2373–2423. https://doi.org/10.1175/MWR-D-11-00121.1

Wood, R., & Bretherton, C. S. (2006). On the relationship between stratiform low cloud cover and lower-tropospheric stability. *Journal of Climate*, 19(24), 6425–6432. https://doi.org/10.1175/JCLI3988.1

Xi, B., Dong, X., Zheng, X., & Wu, P. (2022). Cloud phase and macrophysical properties over the Southern Ocean during the MARCUS field campaign. *Atmospheric Measurement Techniques*, 15(12), 3761–3777. https://doi.org/10.5194/amt-15-3761-2022

Yamaguchi, T., Feingold, G., & Kazil, J. (2019). Aerosol-cloud interactions in trade wind cumulus clouds and the role of vertical wind shear. *Journal of Geophysical Research: Atmospheres*, 124(22), 12244–12261. https://doi.org/10.1029/2019JD031073

Yang, J., Zhao, C., Sun, Y., Chi, Y., & Yang, Y. (2022). Aerosol first indirect effect over narrow longitude regions of North Pacific and same-latitude lands. *Atmospheric Environment*, 277, 119081. https://doi.org/10.1016/j.atmosenv.2022.119081

Yu, L., Zhang, M., Wang, L., Li, H., & Li, J. (2024). Characteristics of aerosols and clouds and their role in Earth's energy budget. *Journal of Climate*, 37(3), 995–1014. https://doi.org/10.1175/JCLI-D-23-0414.1

Zheng, X., Xi, B., Dong, X., Logan, T., Wang, Y., & Wu, P. (2020). Investigation of aerosol-cloud interactions under different absorptive aerosol regimes using Atmospheric Radiation Measurement (ARM) Southern Great Plains (SGP) ground-based measurements. *Atmospheric Chemistry and Physics*, 20(6), 3483–3501. https://doi.org/10.5194/acp-20-3483-2020

References From the Supporting Information

Chakraborty, S., Schiro, K. A., Fu, R., & Neelin, J. D. (2018). On the role of aerosols, humidity, and vertical wind shear in the transition of shallow-to-deep convection at the Green Ocean Amazon 2014/5 site. *Atmospheric Chemistry and Physics*, 18(15), 11135–11148. https://doi.org/10.5194/acp-18-11135-2018

Gandham, H., Dasari, H. P., Karumuri, A., Ravuri, P. M. K., & Hoteit, I. (2022). Three-dimensional structure and transport pathways of dust aerosols over West Asia. *npj Climate and Atmospheric Science*, 5(1), 45. https://doi.org/10.1038/s41612-022-00266-2

Han, Y., Wang, T., Tang, J., Wang, C., Jian, B., Huang, Z., & Huang, J. (2022). New insights into the Asian dust cycle derived from CALIPSO lidar measurements. *Remote Sensing of Environment*, 272, 112906. https://doi.org/10.1016/j.rse.2022.112906

Jeong, J.-H., Witte, M. K., & Smalley, M. (2023). Effects of wind shear and aerosol conditions on the organization of precipitating marine stratocumulus clouds. *Journal of Geophysical Research: Atmospheres*, 128(24), e2023JD039081. https://doi.org/10.1029/2023JD039081

Mace, G. G., & Zhang, Q. (2014). The CloudSat radar-lidar geometrical profile product (RL-GeoProf): Updates, improvements, and selected results. Jour*nal of Geophysical Research: Atmospheres*, 119(15), 9441–9462. https://doi.org/10.1002/2013JD021374

McErlich, C., McDonald, A., Schuddeboom, A., & Silber, I. (2021). Comparing satellite- and ground-based observations of cloud occurrence over high southern latitudes. *Journal of Geophysical Research: Atmospheres*, 126(6), e2020JD033607. https://doi.org/10.1029/2020JD033607

Platnick, S., Meyer, K. G., King, M. D., Wind, G., Amarasinghe, N., Marchant, B., Arnold, G. T., Zhang, Z., Hubanks, P. A., Holz, R. E., Yang, P., Ridgway, W. L., & Riedi, J. (2017). The MODIS cloud optical and microphysical products: Collection 6 updates and examples from Terra and Aqua. *IEEE Transactions on Geoscience and Remote Sensing*, 55(1), 502–525. https://doi.org/10.1109/TGRS.2016.2610522

Sporre, M. K., O'Connor, E. J., Håkansson, N., Thoss, A., Swietlicki, E., & Petäjä, T. (2016). Comparison of MODIS and VIIRS cloud properties with ARM ground-based observations over Finland. *Atmospheric Measurement Techniques*, 9(7), 3193–3203. https://doi.org/10.5194/amt-9-3193-2016

Stephens, G., Winker, D., Pelon, J., Trepte, C., Vane, D., Yuhas, C., L'Ecuyer, T., & Lebsock, M. (2018). CloudSat and CALIPSO within the A-Train: Ten years of actively observing the Earth system. *Bulletin of the American Meteorological Society*, 99(3), 569–581. https://doi.org/10.1175/BAMS-D-16-0324.1

Wang, T., Han, Y., Huang, J., Sun, M., Jian, B., Huang, Z., & Yan, H. (2020). Climatology of dust-forced radiative heating over the Tibetan Plateau and its surroundings. *Journal of Geophysical Research: Atmospheres*, 125(17), e2020JD032942. https://doi.org/10.1029/2020JD032942

Winker, D. M., Pelon, J., Coakley, J. A., Jr., Ackerman, S. A., Charlson, R. J., Colarco, P. R., Flamant, P., Fu, Q., Hoff, R. M., Kittaka, C., Kubar, T. L., Le Treut, H., McCormick, M. P., Mégie, G., Poole, L., Powell, K., Trepte, C., Vaughan, M. A., & Wielicki, B. A. (2010). The CALIPSO mission: A global 3D view of aerosols and clouds. *Bulletin of the American Meteorological Society*, 91(9), 1211–1229. https://doi.org/10.1175/2010BAMS3009.1

Zhang, Y., Stevens, B., Medeiros, B., & Ghil, M. (2009). Low-cloud fraction, lower-tropospheric stability, and large-scale divergence. *Journal of Climate*, 22(18), 4827–4844. https://doi.org/10.1175/2009JCLI2891.1

Zheng, X., Feng, Y., Painemal, D., Zhang, M., Xie, S., Li, Z., Jacob, R., & Lusch, B. (2025). Regime-based aerosol–cloud interactions from CALIPSO-MODIS and the Energy Exascale Earth System Model version 2 (E3SMv2) over the Eastern North Atlantic. *Atmospheric Chemistry and Physics*, 25(23), 17473–17499. https://doi.org/10.5194/acp-25-17473-2025